

# Quantum Simulation for Dynamical Transition Rates in Open Quantum Systems

Robson Christie<sup>1</sup>, Kyunghyun Baek<sup>2</sup>, Jeongho Bang<sup>2</sup>, Jaewoo Joo<sup>1</sup>

<sup>1</sup>School of Mathematics and Physics, University of Portsmouth, PO1 3FX, United Kingdom.

<sup>2</sup>Institute for Convergence Research and Education in Advanced Technology, Yonsei University, Seoul 03722, Republic of Korea.

Contributing authors: [jaewoo.joo@port.ac.uk](mailto:jaewoo.joo@port.ac.uk);

## Abstract

Estimating transition rates in open quantum systems is a significant challenge in physics and chemistry due to the exponential increase in computational resources required with the system sizes. Addressing this issue, we introduce a novel and efficient quantum simulation method to compute dynamical transition rates in Markovian open quantum systems. This method reformulates the transition rate expression, represented as the time derivatives of correlation functions, into directly measurable quantities in parametrised mixed-state quantum circuits. This approach allows us to estimate the transition rate more accurately without requiring the computation of the correlation function in a dynamical open quantum system. To validate our approach, we perform quantum simulations experimentally on IBMQ quantum processors for a decohering spin-1/2 model, compared with analytic solutions and quantum numerical simulation. Motivated by quantum chemistry-related applications, we examine our method in one-dimensional Caldeira-Leggett quantum Brownian motion model. Through theoretical and numerical analyses, we address the scalability of our scheme and the promise of significant computational advantages over its classical counterpart. Thus, our new approach holds the potential to surpass the bottlenecks of current quantum chemical research, particularly in accurately predicting molecular reaction rates and designing novel materials on the current and the near-term realisable quantum hardware.

**Keywords:** Quantum simulation, Transition rate, Open quantum systems

# Introduction

Quantum simulations have recently emerged as powerful tools for analysing complex systems and dynamics, offering immense potential for applications such as quantum chemistry [1–4], many-body physics [5–7], quantum field theory [8–10], and cosmology [11–13]. Classical simulation methods have made significant strides in studying quantum systems through modern numerical techniques. Despite these remarkable advances, classical techniques face fundamental limitations when scaling to larger quantum systems, as simulating quantum properties becomes exponentially more difficult due to the additional degrees of freedom such as superposition and entanglement [14]. This computational barrier reveals the possibility of achieving practical advantages through quantum simulations on quantum machines, which can naturally accommodate a large quantum system without the exponential resource overhead. Thus, this quantum simulation research enables the exploration of quantum phenomena beyond the horizon of classical counterparts.

To tackle this fundamental obstacle, the primary objective of current quantum simulation efforts is to develop efficient quantum algorithms that can demonstrate practical quantum advantages and to establish mature computing techniques for the eventual transition to noise-robust and fault-tolerant quantum computing. To leverage the capabilities of Noisy Intermediate-Scale Quantum (NISQ) devices despite limited qubit counts and unavoidable quantum noise [15–17], one promising approach involves using master equations to simulate the dynamics of open quantum systems. Master equation approaches account for environmental effects by incorporating their non-unitary characteristics, eliminating the need to simulate every degree of freedom in the entire large quantum system. Quantum simulation methods under master equations not only capture the essential phenomena associated with environmental interactions but could also outperform modern numerical methods for complex open quantum systems [7, 18–23]. Thus, the master equation quantum simulation may offer a new pathway to study dynamical quantum phenomena on NISQ hardware, and the development of these applications could bring an extensive industrial impact with a quantum-enhanced toolkit to simulate generalised master equations in the future [24].

Here, we develop a novel quantum simulation algorithm to compute the key dynamical features for understanding the thermal transitions in many-body open quantum systems: the correlation function and the quantum transition rate. Our quantum simulation method can evaluate the two-point time-correlation function of quantum observables and its rate under Markovian master equation dynamics. Recent progress in quantum simulation has highlighted a growing interest in computing various types of correlation functions in quantum systems [25–33] and also thermal fluctuations within open quantum systems [34–36]. For example, Fig. 1 schematically illustrates that the correlation function in time  $C(t)$  provides extensive information on both macroscopic non-equilibrium and microscopic equilibrium properties through the linear response theory [28, 36, 37]. When two phase-space regions  $A$  and  $B$  correspond to metastable states of the system, the linear response of the non-equilibrium correlation function can be interpreted as  $C(t) \approx k_{ab} t$  with the constant rate  $k_{ab}$  of equilibrium fluctuations. Therefore, by performing master equation simulations of non-equilibrium relaxation

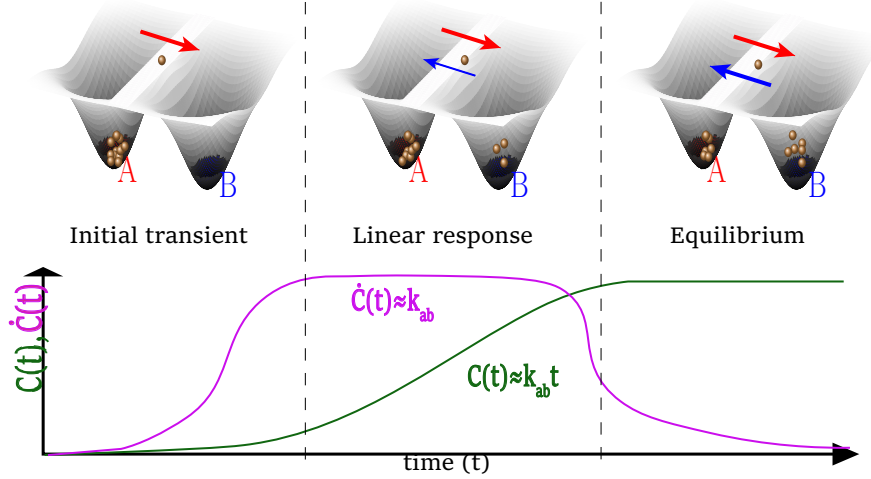


**Fig. 1:** Illustration of typical phases of metastable transition dynamics. After an initial transient from  $A$ , the correlation function  $C(t)$  (green) exhibits linear growth in the middle process before saturating at equilibrium. The time derivative of the correlation function (violet) shows its transient behaviour before plateauing with the rate constant in non-equilibrium as  $\dot{C}(t) \approx k_{ab}$ , then decaying to zero toward equilibrium.

over relatively short times, we can estimate the correlation function as well as the transition rate of equilibrium fluctuations as the time derivative of the correlation function  $\dot{C}(t)$ . The importance of evaluating  $C(t)$  and  $\dot{C}(t)$  has been emphasised in the study of classical molecular dynamics [38–40], and also its quantum contexts [41–44]. However, stochastic numerical computations are in general requested for long-time simulation to analyse open quantum systems.

Building on this perspective, our quantum algorithm provides the correlation function as well as the time derivative of the correlation function via the expectation values of single-qubit measurements in parametrised mixed-state quantum circuits. To be efficient methods in quantum simulation, it is imperative to select measurement observables that encode the maximum amount of dynamical information while designing quantum simulators to estimate their quantities in a way that minimises the number of qubit measurements required for statistical confidence. To validate the feasibility of our method, we first perform a proof-of-principle quantum algorithm for a single-spin open quantum system. Herein, we run the six-qubit simulation on an IBMQ machine for evaluating  $C(t)$  and  $\dot{C}(t)$ . The experimental results show particularly impressive agreement with the analytical solutions and ideal quantum numerical simulations. We extend our method to a chemistry-motivated quantum model known as the Caldeira-Legget (CL) model of quantum Brownian motion [45, 46]. By performing 16-qubit numerical simulations, we demonstrate that our methods enable to estimate  $C(t)$  and  $\dot{C}(t)$  values aligning well with those from the direct numerical integration of ideal Lindblad dynamics. Moreover, the estimated curve of  $\dot{C}(t)$  clearly

captures the detailed quantum phenomena of this dynamical transition. Therefore, we believe that the proposed quantum simulation approach brings significantly enhanced computational efficiency and robust scalability for exploring 2D and 3D open quantum systems and is well-suited for investigating more complex, and classically-prohibitive, real-world problems.

## Lindblad evolution in an open quantum system

The theory of open quantum systems describes the behaviour of a system of interest interacting with its environment in terms of effective non-unitary dynamics. Any Markovian quantum dynamics that preserves the trace, positivity, and Hermiticity of the density operator can be expressed in a Lindblad equation [47–49]. In contrast to the closed-system Schrödinger equation, the Lindblad equation can describe non-unitary processes such as decoherence and dissipation, which are the irreversible exchange of information or energy between the system and its environment. This equation for the system state as a density matrix  $\hat{\rho}_S$  is written in

$$\frac{d}{dt}\hat{\rho}_S = \mathcal{L}(\hat{\rho}_S(t)) = -\frac{i}{\hbar}[\hat{H}, \hat{\rho}_S] + \frac{1}{\hbar} \sum_k \left( \hat{L}_k \hat{\rho}_S \hat{L}_k^\dagger - \frac{1}{2} \{ \hat{\rho}_S, \hat{L}_k^\dagger \hat{L}_k \} \right), \quad (1)$$

where  $\hat{H}$  is the system Hamiltonian responsible for unitary dynamics, and  $\hat{L}_k$  are the Lindblad operators for the integer  $k$ , associated with decohering and dissipative quantum dynamics. In the case of Hermitian Lindblad operators ( $\hat{L}_k^\dagger = \hat{L}_k$ ), the equation is involved with dephasing or pure decoherence processes while non-Hermitian Lindblad operators can describe quantum dissipative processes and thermal systems [50].

## Quantum correlation functions and their derivatives

Let us briefly recall the theory of quantum time-correlation functions [39, 51]. To define the states in the domains  $A$  and  $B$  and their transitions, we first determine the coordinate quantum state  $|x\rangle$  in the Hilbert space of the system, with its projection operator given by  $|x\rangle\langle x|$ . Then, the projection observables are defined in the coordinate domains  $A$  and  $B$  as

$$\hat{\theta}_K = \int_{x \in K} dx |x\rangle\langle x|, \quad (2)$$

for  $K = A, B$  (see Fig. 1). The quantum time-correlation function between  $\hat{\theta}_A$  and  $\hat{\theta}_B$  and its derivative in time (from initial time 0 to  $t$ ) are given by

$$C_{\mathbb{C}}(t) \equiv \frac{\langle \hat{\theta}_A(0) \hat{\theta}_B(t) \rangle_{eq}}{\langle \hat{\theta}_A(0) \rangle_{eq}}, \quad \text{and} \quad \dot{C}_{\mathbb{C}}(t) \equiv \frac{\langle \hat{\theta}_A(0) \dot{\hat{\theta}}_B(t) \rangle_{eq}}{\langle \hat{\theta}_A(0) \rangle_{eq}}, \quad (3)$$

where  $\mathbb{C}$  signifies a complex value. The real part of  $\dot{C}_{\mathbb{C}}(t)$  represents the quantum transition rate from  $A$  to  $B$  while the imaginary component contains phase information [51].  $\langle \cdot \rangle_{eq}$  represents the average of the operator inside over the equilibrium distribution. Since both quantum observables  $\hat{\theta}_A$  and  $\hat{\theta}_B$  are Hermitian, the real component

of the correlation function can be expressed as

$$C(t) \equiv \frac{\langle \{\hat{\theta}_A(0), \hat{\theta}_B(t)\} \rangle_{eq}}{2\langle \hat{\theta}_A(0) \rangle_{eq}}, \quad (4)$$

where  $\{\cdot, \cdot\}$  is the anti-commutator, and the transition rate expression becomes

$$\dot{C}(t) = \frac{\langle \{\hat{\theta}_A(0), \dot{\hat{\theta}}_B(t)\} \rangle_{eq}}{2\langle \hat{\theta}_A(0) \rangle_{eq}} = \frac{\text{Tr}(\hat{\rho}_{eq} \{ \hat{\theta}_A(0), \mathcal{L}^\dagger(\hat{\theta}_B(t)) \})}{2\text{Tr}(\hat{\rho}_{eq} \hat{\theta}_A(0))}, \quad (5)$$

where  $\hat{\theta}_B(t) = e^{\mathcal{L}^\dagger t}(\hat{\theta}_B(0))$  is called the Heisenberg picture Lindblad (Heisenberg-Lindblad) time evolution. Note that  $\hat{\rho}_{eq}$  is the equilibrium state of the Lindblad dynamics. The dynamics of observable  $\hat{\theta}_B(t)$  in  $\dot{C}(t)$  is governed by the Lindblad equation in the Heisenberg picture such as

$$\frac{d}{dt}\hat{\theta}_B(t) = \mathcal{L}^\dagger(\hat{\theta}_B(t)) = \frac{i}{\hbar} [\hat{H}, \hat{\theta}_B(t)] + \frac{1}{\hbar} \sum_k \left( \hat{L}_k^\dagger \hat{\theta}_B(t) \hat{L}_k - \frac{1}{2} \{ \hat{\theta}_B(t), \hat{L}_k^\dagger \hat{L}_k \} \right). \quad (6)$$

The further detail derivations are given in the Supplementary Information.

## Results

### Transition rate algorithm in the Heisenberg picture

Fig. 2 illustrates our transition rate quantum circuit, which evaluates the correlation function and the transition rate in terms of the expectation values from the control qubit measurements. Due to the mixed-state paradigm, we use the density operator representation after stage  $n$  denoted as  $\hat{\Phi}_n$ . Initially, the prepared input form is

$$\hat{\Phi}_0 = \hat{c}_+ \otimes \hat{\theta}_B \otimes \hat{\theta}_A \otimes \hat{\rho}_{eq}, \quad (7)$$

where the control qubit is given such that  $\hat{c}_+ = |+\rangle\langle +|$  with  $|+\rangle = (|0\rangle + |1\rangle)/\sqrt{2}$ . Note that the observables  $\hat{\theta}_A$  and  $\hat{\theta}_B$  are given in a discretised representation on the quantum circuit and can be regarded as the mixed states along with the equilibrium state  $\hat{\rho}_{eq}$  (see their notations in Methods). At the first stage, a phase-shifted rotation- $\hat{\sigma}_z$  operator  $\hat{R}(\chi)$  is applied with parameter  $\chi$  in the control qubit

$$\hat{R}(\chi) = e^{-i\chi(\hat{\sigma}_z - 1)/2}. \quad (8)$$

We require two modular quantum circuits such as the Heisenberg-Lindblad evolution gate  $e^{\mathcal{L}^\dagger t}$  and the mS gate for  $\hat{\Phi}_1$  in Fig. 2. An initial observable  $\hat{\theta}_B$  evolves over time  $t$  under the Heisenberg-Lindblad dynamics, resulting in the operator  $\hat{\theta}_B(t) = e^{\mathcal{L}^\dagger t}(\hat{\theta}_B)$ . Inspired by [22], an ancillary qudit with  $d + 1$  dimensions is used with  $d$

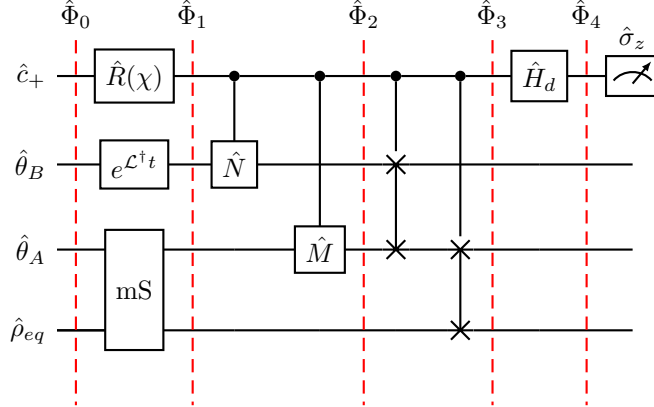


**Fig. 2:** Illustration of the transition rate quantum circuit in the Heisenberg picture. We denote the total density operator  $\hat{\Phi}_n$  at stage  $n$ . After  $\hat{\Phi}_4$ , one only measures the control qubit in  $z$ -axis.

Lindblad operators in the evolution gate as shown in Methods. For example, the case of a single Lindblad operator requires a single ancillary qubit inside the modular evolution gate. We mainly examine the modular evolution circuit with a fixed time step  $N$ , implying  $N$  iterations of the modular circuit to create  $\hat{\theta}_B(t)$ , and the number of the time step can be independently determined with the system sizes. At the left bottom of Fig. 2, another modular circuit, named a mixed SWAP (mS) gate, is performed between the two lower channels as

$$\hat{\theta}_A \otimes \hat{\rho}_{eq} \xrightarrow{\text{mS}} \frac{1}{2} \left( \hat{\theta}_A \otimes \hat{\rho}_{eq} + \hat{\rho}_{eq} \otimes \hat{\theta}_A \right). \quad (9)$$

This mS gate can be implemented by stochastically swapping the lower two quantum channels. Alternatively, we can add an extra control qubit in  $|+\rangle$  inside the mS gate and perform a controlled-SWAP (C-SWAP) on  $\hat{\theta}_A$  and  $\hat{\rho}_{eq}$ . By tracing out the control qubit inside the mS gate, we obtain the equal mixture of  $\hat{\theta}_A$  and  $\hat{\rho}_{eq}$  for  $\hat{\Phi}_1$ . Note that the C-SWAP gate is derived for mixed states in the Supplementary Information.

In Fig. 2, after the controlled- $\hat{N}$  and  $-\hat{M}$  gates for  $\hat{\Phi}_2$ , we apply two sequential C-SWAP gates to achieve  $\hat{\Phi}_3$ , and its detailed scheme can be found in [23]. Finally, after the last Hadamard gate  $\hat{H}_d$  in the control qubit, we measure this qubit along the  $z$ -axis at  $\hat{\Phi}_4$ . The statistics of the single-qubit measurements provide us the expectation value  $\mathcal{E}$  as follows

$$\mathcal{E} = \text{Tr} \left( \hat{\sigma}_z^c \hat{\Phi}_4 \right) = \frac{1}{2} \left\langle e^{-i\chi} \{ \hat{\theta}_A, \hat{M}^\dagger \hat{\theta}_B(t) \hat{N}^\dagger \} + e^{i\chi} \{ \hat{\theta}_A, \hat{N} \hat{\theta}_B(t) \hat{M} \} \right\rangle_{eq}. \quad (10)$$

Note that the trace-out with  $\hat{\sigma}_z^c$  implies the measurements of the control qubit along the  $z$ -axis, and the detail derivation of  $\mathcal{E}$  is provided in the Supplementary Information. For the simplest case with  $\chi = 0$ ,  $\hat{N} = \mathbb{I}$ , and  $\hat{M} = \mathbb{I}$  in the quantum circuit, the statistics of single-qubit measurements gives us the upper part of the correlation function such

as

$$\mathcal{E}_C = \text{Tr}(\hat{\sigma}_z^c \hat{\Phi}_4) = \left\langle \{\hat{\theta}_A, \hat{\theta}_B(t)\} \right\rangle_{eq}. \quad (11)$$

By varying the phase gate parameter  $\chi$  and the two controlled-operator gates, we can reproduce the expectation values of the terms in Eq. (5) with  $\hat{\theta}_B(t)$  evolving under the Lindblad dynamics in Eq. (6). In the transition rate quantum circuit, we set the parameters  $\chi = -\pi/2$ ,  $\hat{N} = \mathbb{I}$ , and  $\hat{M} = \hat{H}$  and the first expectation value for the Hamiltonian terms in Eq. (6) with the anti-commutator is given by

$$\mathcal{E}_H = \frac{2}{\hbar} \text{Tr}(\hat{\sigma}_z^c \hat{\Phi}_4) = \frac{i}{\hbar} \left\langle \{\hat{\theta}_A, [\hat{H}, \hat{\theta}_B(t)]\} \right\rangle_{eq}. \quad (12)$$

If we set up  $\chi = 0$ ,  $\hat{N} = \hat{L}_k^\dagger$ , and  $\hat{M} = \hat{L}_k$  for the jump term, the second expectation value is equal to

$$\mathcal{E}_J = \frac{1}{\hbar} \text{Tr}(\hat{\sigma}_z^c \hat{\Phi}_4) = \frac{1}{\hbar} \left\langle \{\hat{\theta}_A, \hat{L}_k^\dagger \hat{\theta}_B(t) \hat{L}_k\} \right\rangle_{eq}. \quad (13)$$

For the double anti-commutator terms, we put the parameters of  $\chi = 0$ ,  $\hat{N} = \mathbb{I}$  and  $\hat{M} = \hat{L}_k^\dagger \hat{L}_k$  and the third expectation value is

$$\mathcal{E}_{AC} = -\frac{1}{\hbar} \text{Tr}(\hat{\sigma}_z^c \hat{\Phi}_4) = -\frac{1}{2\hbar} \left\langle \{\hat{\theta}_A, \{\hat{\theta}_B(t), \hat{L}_k^\dagger \hat{L}_k\}\} \right\rangle_{eq}. \quad (14)$$

Finally, if we remove the channel  $\hat{\theta}_B$  related part and the mS gate in Fig. 2, the quantum circuit with  $\chi = 0$ ,  $\hat{N} = \mathbb{I}$ , and  $\hat{M} = \mathbb{I}$  provides the denominator term of  $C(t)$  and  $\dot{C}(t)$  such as

$$\mathcal{E}_D = \text{Tr}(\hat{\sigma}_z^c \hat{\Phi}_4) = \left\langle \hat{\theta}_A \right\rangle_{eq}. \quad (15)$$

Therefore, the correlation function is simply given by  $C(t) = \mathcal{E}_C / (2\mathcal{E}_D)$  and the quantum transition rate from  $\hat{\theta}_A$  to  $\hat{\theta}_B$  in Eq. (5) is evaluated by the combination of four expectation values such as

$$\dot{C}(t) = \frac{\mathcal{E}_H + \sum_k (\mathcal{E}_J + \mathcal{E}_{AC})}{2\mathcal{E}_D}. \quad (16)$$

## Spin-1/2 model

We examine a simple spin-1/2 example of an open quantum system to benchmark our scheme since the system is analytically solvable: a single spin-1/2 system subject to a magnetic field of strength  $\mu$  in the  $y$ -axis, undergoing a  $z$ -component measurement with coupling strength  $\gamma$  as an environmental effect (see the schematic figure in the Supplementary Information). This physical system is governed by a Lindblad equation with a Hamiltonian and a Hermitian Lindblad operator in Eq. (6) such as

$$\hat{H} = \mu \hat{\sigma}_y \quad \text{and} \quad \hat{L} = \sqrt{\gamma} \hat{\sigma}_z. \quad (17)$$

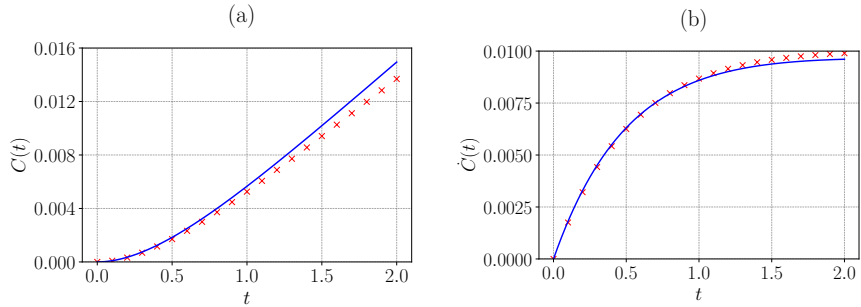


**Fig. 3:** Spin-1/2 correlation function  $C(t)$  in (a) and its rate  $\dot{C}(t)$  in (b) with respect to evolution time  $t$ . For  $\mu = 0.1$ ,  $\gamma = 1$  and  $\hbar = 1$ , the analytic results are plotted in blue lines, and red crosses indicate the data of quantum numerical simulation with 25 time steps in the modular Heisenberg-Lindblad evolution circuit  $e^{\mathcal{L}^\dagger t}$  in Fig. 2.

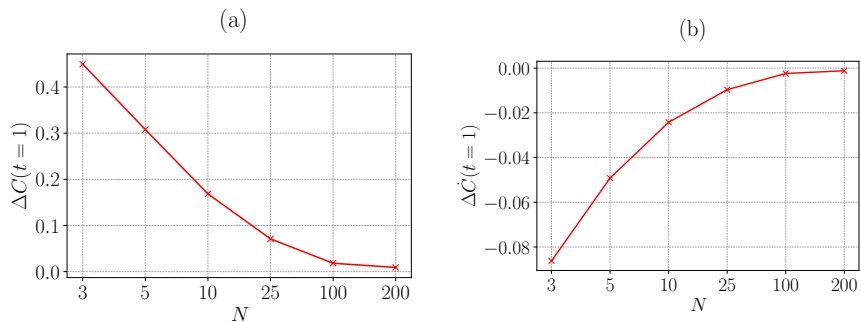


**Fig. 4:** Spin-1/2 relative error of the correlation function (a) and rate (b) at  $t = 1$  with respect to the number of time steps  $N$  (e.g.,  $N$  recycles of an ancillary qubit) used in the Heisenberg-Lindblad evolution with the same parameters in Fig. 3. The relative errors are calculated by subtracting the simulated value from the analytic value and dividing by the analytic value, i.e.  $\Delta C = (C_{ana} - C_{sim})/C_{ana}$  and  $\Delta \dot{C} = (\dot{C}_{ana} - \dot{C}_{sim})/\dot{C}_{ana}$ .

In particular, when  $\mu$  is significantly smaller than  $\gamma$ , states  $|0\rangle$  and  $|1\rangle$  exhibit metastability and we can choose the observables  $\hat{\theta}_A = |0\rangle\langle 0|$  and  $\hat{\theta}_B = |1\rangle\langle 1|$  in this regime to define the transition rate between them. Then, the equilibrium state of this system is known as a fully mixed spin state as

$$\hat{\rho}_{eq} = \frac{1}{2} (|0\rangle\langle 0| + |1\rangle\langle 1|). \quad (18)$$



Thus, the analytic expressions for the correlation function and the transition rate are given in

$$C(t) = \frac{1}{2} \left( 1 - e^{-\frac{\gamma}{\hbar}t} \left( \cosh(\omega t) + \frac{\gamma}{\hbar\omega} \sinh(\omega t) \right) \right), \quad (19)$$

$$\dot{C}(t) = \frac{2\mu^2}{\hbar^2\omega} e^{-\frac{\gamma}{\hbar}t} \sinh(\omega t), \quad (20)$$

with  $\omega = \sqrt{(\gamma^2 - 4\mu^2)/\hbar^2}$  (see the details in Methods).

In Fig. 3, we present the analytic solutions in solid blue lines and the results of quantum numerical simulations at different  $t$  in red crosses using QuTiP [52]. The results of quantum numerical simulation are generated by performing single-qubit measurements in Fig. 2. The modular time evolution gate  $e^{\mathcal{L}^\dagger t}$  here serves as a proof-of-concept for the Heisenberg-Lindblad evolution method, utilising 25 time-step iterations ( $N = 25$  at each  $t$ ) with recycling a single ancillary qubit (equivalently 25 ancillary qubits without recycling) in Figs. 3 (a) and (b). Since the discretised evolution period in each time step is given by  $\delta = t/N$ , we have a more accurate evolved operator  $\hat{\theta}_B(t)$  with smaller  $t$  due to the fixed  $N$  (see details in Methods). In Fig. 4, the discrepancies between the analytical solutions and quantum numerical simulations approach zero at  $t = 1$  as  $N$  increases. This implies the fact that the shorter time duration  $\delta$  (equivalent to larger  $N$ ) builds a more ideal  $\hat{\theta}_B(t)$  at time  $t$  in the modular evolution gate and provides more accurate results of  $C(t)$  and  $\dot{C}(t)$ .

## Experimental results for the spin-1/2 model

For the quantum experimental simulation of the spin-1/2 model, we also developed the Schrödinger picture derivative circuit shown in Fig. 5, which is an alternative quantum circuit to Fig. 2. While the Heisenberg picture derivative circuit provides an intuitive expression for the transition rate in Eq. (5), it requires a minimum of three sets of the system size qubits with two C-SWAP gates (not counting the ancillary qubits required for the Heisenberg-Lindblad evolution  $e^{\mathcal{L}^\dagger t}$ ) shown in Fig. 2. In contrast, the Schrödinger picture derivative circuit reduces the requirement to only two sets of the system qubits with a single C-SWAP gate shown in Fig. 5. Thus, this makes us the experimental feasibility of our scheme for the spin-1/2 system on IBMQ machines.

The trade-off in switching to the Schrödinger picture circuit is the need to build a new controlled-projector gate (controlled- $\hat{\theta}_A$  operator) acting on  $\hat{\rho}_{eq}$ . We note that the controlled- $\hat{N}$  and  $-\hat{M}$  gates are unitary for this spin-1/2 case, however, the controlled- $\hat{\theta}_A$  operator is non-unitary, which can be decomposed into a sum of controlled-unitary gates. As an example, the controlled- $\hat{\theta}_A$  gate is implemented by the sum of two identity operators and a controlled- $\hat{\sigma}_z$  gate in our experiments such as

$$|0\rangle\langle 0| \otimes \mathbb{I} + |1\rangle\langle 1| \otimes \hat{\theta}_A = \frac{1}{2} \mathbb{I} \otimes \mathbb{I} + \frac{1}{2} (|0\rangle\langle 0| \otimes \mathbb{I} + |1\rangle\langle 1| \otimes \hat{\sigma}_z). \quad (21)$$

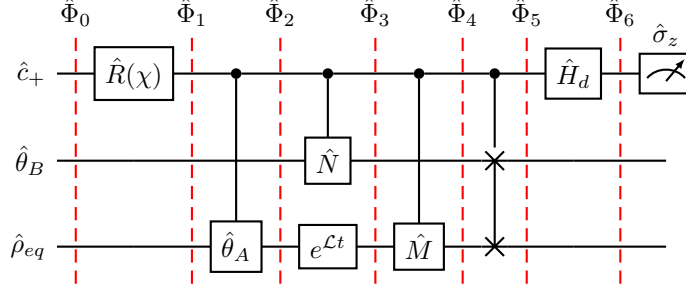


**Fig. 5:** Schrödinger picture derivative circuit equivalent to Fig. 2.

As shown in Table 1, we can analytically calculate the expectation values with different parameters and obtain the transition rate in the Schrödinger picture as

$$\dot{C}(t) = \frac{\mathcal{E}_{H1} + \mathcal{E}_{H2} + \mathcal{E}_J + \mathcal{E}_{AC1} + \mathcal{E}_{AC2}}{2\mathcal{E}_D}. \quad (22)$$

For the experiments, we run our algorithm with six qubits on the IBMQ (*ibm\_brisbane*) machine [53]. Three qubits were assigned to  $\hat{\theta}_B$ ,  $\hat{\rho}_{eq}$ , and the control qubit  $\hat{c}_+$  in Fig. 5 while the other three qubits ( $A_1$ – $A_3$ ) were used for three iterations of the ancillary qubit in the modular Schrödinger-Lindblad evolution gate  $e^{\mathcal{L}t}$  (see the details in Methods). Fig. 6 (a) presents the experimental results of the correlation function  $C(t)$  with ten sets of 20,000 shots at each  $t$  along with the ideal six-qubit numerical simulation without noise and the analytical solution in Eq. (19). The experimental values of  $C(t)$  show relatively large error bars, but we find that its curve tends to increase with respect to time  $t$  as we can expect from the analytical and numerical results. However, the analytical and numerical values of  $C(t)$  are much smaller than

Term	$\chi$	$\hat{N}$	$\hat{M}$	$\hat{\theta}_A$	$\mathcal{E}$
$\mathcal{E}_{H1}$	$-\frac{\pi}{2}$	$\mathbb{I}$	$\hat{H} = \mu\hat{\sigma}_y$	$\mathbb{I}$ $\hat{\sigma}_z$	$0$ $\frac{\mu^2}{\hbar^2\omega}e^{-\frac{\gamma}{\hbar}t}\sinh(\omega t)$
$\mathcal{E}_{H2}$	$\frac{\pi}{2}$	$\hat{H} = \mu\hat{\sigma}_y$	$\mathbb{I}$	$\mathbb{I}$ $\hat{\sigma}_z$	$0$ $\frac{\mu^2}{\hbar^2\omega}e^{-\frac{\gamma}{\hbar}t}\sinh(\omega t)$
$\mathcal{E}_J$	0	$\hat{L}^\dagger = \sqrt{\gamma}\hat{\sigma}_z$	$\hat{L} = \sqrt{\gamma}\hat{\sigma}_z$	$\mathbb{I}$ $\hat{\sigma}_z$	$-\frac{\gamma}{2\hbar}e^{-\frac{\gamma}{\hbar}t}\left(\cosh(\omega t) + \frac{\gamma}{\hbar\omega}\sinh(\omega t)\right)$
$\mathcal{E}_{AC1}$	0	$\mathbb{I}$	$\hat{L}^\dagger\hat{L} = \gamma\mathbb{I}$	$\mathbb{I}$ $\hat{\sigma}_z$	$\frac{\gamma}{4\hbar}e^{-\frac{\gamma}{\hbar}t}\left(\cosh(\omega t) + \frac{\gamma}{\hbar\omega}\sinh(\omega t)\right)$
$\mathcal{E}_{AC2}$	0	$\hat{L}^\dagger\hat{L} = \gamma\mathbb{I}$	$\mathbb{I}$	$\mathbb{I}$ $\hat{\sigma}_z$	$\frac{\gamma}{4\hbar}e^{-\frac{\gamma}{\hbar}t}\left(\cosh(\omega t) + \frac{\gamma}{\hbar\omega}\sinh(\omega t)\right)$

**Table 1:** Analytic expressions contributing to  $\dot{C}(t)$  in Eq. (22). We have summed over equally with  $|0\rangle\langle 0|$  and  $|1\rangle\langle 1|$  contributions to  $\hat{\rho}_{eq}$  for each entry in the rightmost column. The operator  $\hat{\theta}_A$  is implemented by the combination of  $\mathbb{I}$  and  $\hat{\sigma}_z$ . Further details of the expectation value terms are given in the Supplementary Information.

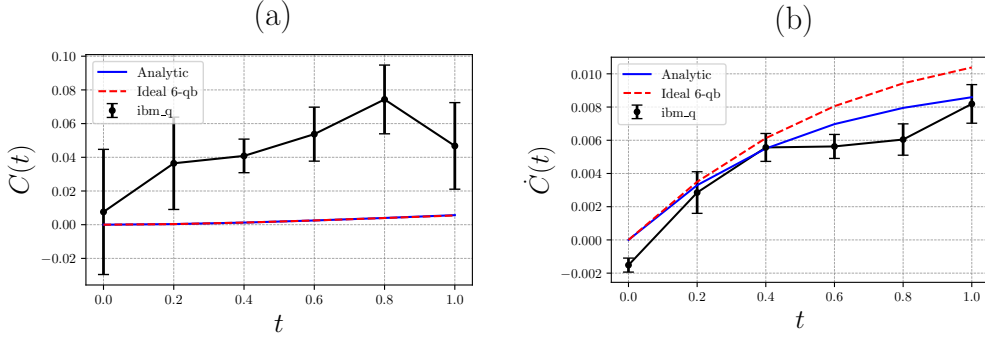


**Fig. 6:** The IBMQ experimental data of  $C(t)$  with ten sets of 20,000 shots for discretised time  $t$  in (a) and of  $\dot{C}(t)$  with five sets of 20,000 shots in (b) are compared to the analytic solution and the ideal six-qubit simulation. For both plots at  $t = \{0, 0.2, 0.4, 0.6, 0.8, 1.0\}$ , the parameters are the same in Fig. 3, and the detail data sets are provided in the Supplementary Information.

the experimental data and are shown beyond the error bars of the experimental data in Fig. 6 (a). Note that we simply assume that  $\mathcal{E}_D = 1/2$  in experiments due to its time independence.

Notably, Fig. 6 (b) displays the experimental results with five sets of 20,000 shots at each  $t$  for the transition rate  $\dot{C}(t)$  alongside the ideal six-qubit numerical simulation as well as the analytical solution in Eq. (20). We observe that the experimental value of  $\dot{C}(t)$  at  $t = 0$  starts from a slightly negative value but the overall shape of the experimental curve of  $\dot{C}(t)$  follows well the analytical and ideal ones. As shown in the Supplementary Information, the systematic shifted values of  $\dot{C}(t)$  are naturally fit to the ideal six-qubit results with small deviations. Thus, we believe that the overall shifted discrepancy between the ideal and experimental results is mainly caused by decoherence and imperfect gate/measurement operations, particularly even in the absence of the time evolution gate on the IBMQ device (see the dashed box  $e^{\mathcal{L}t} = \mathbb{I}$  at  $t = 0$  in Fig. 10).

Moreover, the experimental data of  $\dot{C}(t)$  demonstrate reduced standard errors even with the data sets half the size compared to the experimental results of  $C(t)$ , and the reasons for the error reduction might be two fold. First, it is sufficient to estimate only one of the five expectation values (named  $\mathcal{E}_{H_1}$  in the Table 1) with  $\chi = -\pi/2$ ,  $\hat{N} = \mathbb{I}$ , and  $\hat{M} = \hat{H} = \mu\hat{\sigma}_y$  in Fig. 5. Thus, we only have the error contribution from one of the expectation values in Eq. (22). Second, the variances of experimental data in  $\dot{C}(t)$  can be reduced by exploiting the small parameter  $\mu$ , which can be factored out of the expectation value  $\mathcal{E}_{H_1}$  such as

$$\dot{C}(t) = 2\mathcal{E}_{H_1} = 2\mu\mathcal{E}_{\tilde{H}_1}, \quad (23)$$

where  $\mathcal{E}_{\tilde{H}_1}$  is the expectation value with the Hamiltonian  $\tilde{H} = \hat{\sigma}_y$ . Since  $\mu = 0.1$  in our experiments, the error variance of  $\dot{C}(t)$  from  $\mathcal{E}_{\tilde{H}_1}$  could be in principle ten times

smaller than that from  $\mathcal{E}_{H1}$ . Using the IBM Qiskit emulators [54], we have also verified that both the correlation function and the transition rate converge to the ideal six-qubit curves as the number of shots increases. Therefore, in this specific case with small  $\mu$ , the evaluation of  $\dot{C}(t)$  shows a clear benefit in experiments.

## Caldeira-Leggett model in a 1D double well

We investigate a notable example of an open many-body quantum system closely related to quantum chemistry applications. In the system, a quantum particle is coupled to an environment in the 1D double-well potential. In the seminal work [45], Caldeira and Leggett derived the governing master equation for the reduced density matrix of such a quantum particle interacting with a bath of thermal oscillators known as the quantum Brownian motion. However, the dynamics of the original CL master equation does not preserve the positivity of the reduced density matrix  $\hat{\rho}_S$ , particularly at low temperatures (see the details in the Supplementary Information). The positivity issue can be resolved by adding an extra term, but negligible in the high-temperature regime, in the master equation [46], and this allows the modified CL master equation to be recast in the Lindblad form with an effective Hamiltonian  $\hat{H}_\gamma$  and a non-Hermitian Lindblad operator  $\hat{L}_\gamma$  is given by

$$\frac{d}{dt}\hat{\rho}_S = -\frac{i}{\hbar}[\hat{H}_\gamma, \hat{\rho}_S] + \frac{1}{\hbar}\left(\hat{L}_\gamma\hat{\rho}_S\hat{L}_\gamma^\dagger - \frac{1}{2}\{\hat{\rho}_S, \hat{L}_\gamma^\dagger\hat{L}_\gamma\}\right), \quad (24)$$

with

$$\hat{H}_\gamma = \frac{\hat{P}^2}{2m} + \hat{V}(\hat{X}) + \frac{\gamma}{2}(\hat{X}\hat{P} + \hat{P}\hat{X}), \quad \text{and} \quad \hat{L}_\gamma = \sqrt{\gamma}\left(\lambda_T^{-1}\hat{X} + i\lambda_T\hat{P}\right), \quad (25)$$

where  $\hat{X}$  and  $\hat{P}$  are the position and momentum operators with  $\lambda_T = \sqrt{\hbar/4mk_B T}$ .

In the CL model simulations, we use a discrete position basis and represent the wave function using  $n$  qubits over the coordinate interval  $x \in [0, 1 - 2^{-n}]$ . Each grid point corresponds to its  $n$ -bit binary decimal representation [55] and the grid spacing is given by  $\delta x = 2^{-n}$ . We define the projection operators  $\hat{\theta}_A$  and  $\hat{\theta}_B$  to isolate specific spatial regions within the coordinate interval in each well of the 1D double-well potential such as

$$\hat{\theta}_A \equiv \sum_{0.125 \leq x_k \leq 0.25} |x_k\rangle \langle x_k| \quad \text{and} \quad \hat{\theta}_B \equiv \sum_{0.75 \leq x_k \leq 0.875} |x_k\rangle \langle x_k|, \quad (26)$$

where  $x_k$  denotes the coordinate associated with the  $k$ -th grid point. In the simulations of the Heisenberg picture derivative circuit and the direct numerical integration of ideal Lindblad dynamics, we used  $n = 5$  and the 1D double-well potential is formed by

$$\hat{V}(\hat{X}) = \sum_k 20(x_k - 0.2)^2(x_k - 0.8)^2 |x_k\rangle \langle x_k|. \quad (27)$$

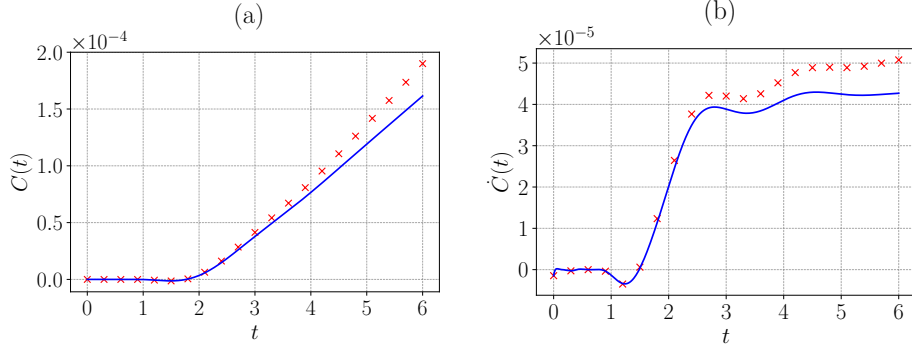


**Fig. 7:** CL correlation function in (a), and the transition rate in (b) with  $m = 1$ ,  $k_B T = 0.0162$  and  $\hbar = 0.01$  ( $k_B$ : Boltzmann constant and  $T$ : temperature). We plot direct numerical results in blue solid lines and the numerical results from the Heisenberg picture derivative circuit in Fig. 2 with 25,000 time steps in red crosses.

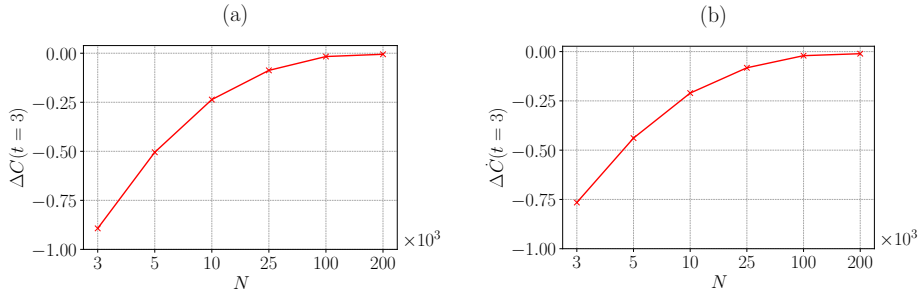


**Fig. 8:** CL relative errors of  $C(t)$  in (a) and  $\dot{C}(t)$  in (b) at  $t = 3$  with respect to the number of time steps  $N$  used in the Heisenberg-Lindblad evolution. The parameters are used as same as Fig. 7 and the relative error formulas are given in Fig. 4.

with a corresponding to a potential energy difference between minima and maxima of  $V_B = 0.162$ , which set the temperature to one tenth of the barrier height such as

$$k_B T = 0.1 V_B. \quad (28)$$

In Figs. 7 (a) and (b), we present the numerical results of  $C(t)$  and  $\dot{C}(t)$  from the quantum circuit in Fig. 2 as red crosses, while the ideal results of the direct numerical calculation are plotted with blue solid lines. Note that we set the parameters of  $m = 1$ ,  $k_B T = 0.0162$ , and  $\hbar = 0.01$  in these simulations. For representing the position  $|x\rangle$ , we use 32 grid points to compute the quantities with reasonable precision in the 1D double well (see details in in Methods). In the quantum numerical simulation, each density operator is represented by 5 qubits equivalent to a  $32 \times 32$  matrix size. The quantum circuit is performed with 16 qubits in total, consisting of a control qubit and three groups of 5-qubit systems in the Heisenberg picture. We use the modular

Heisenberg-Lindblad evolution with  $N = 25,000$  with the 5-qubit system for  $0 \leq t \leq 6$ . The results of quantum numerical simulation show approximate agreement with the errorless direct numerics and capture the detailed features of  $\dot{C}(t)$ . We also observed that the results of the 16-qubit numerical simulation with perfectly prepared  $\hat{\theta}_B(t)$ , accurately match all contributions to  $\dot{C}(t)$  given by the direct numerical integration method.

Remarkably, Fig. 7 (b) reveals small fluctuations in  $\dot{C}(t)$  between  $1 \leq t \leq 2$  and these values of  $\dot{C}(t)$  clearly arise from the rapid relaxation of the initially prepared non-equilibrium state within its initial metastable well in  $A$ . The relaxation process across both wells occurs on a longer time scale, contributing to the linear response and a constant transition rate near  $t = 3$ . These sophisticated quantum effects during the initial transient stage are more prominently reflected in the transition rate curve  $\dot{C}(t)$  in (b) than in the correlation function  $C(t)$  in (a). In Fig. 8, we plot the relative errors at  $t = 3$  for  $C(t)$  and  $\dot{C}(t)$ , and these errors again approach zero as  $N$  increases because of preparing more ideal  $\hat{\theta}_B(t)$ . Further details on the CL model are provided in the Supplementary Information.

## Discussion

We propose a novel quantum algorithm designed to directly estimate the correlation function  $C(t)$  and the time derivative of the correlation function  $\dot{C}(t)$ , interpreted as the transition rate, in an open quantum system governed by the Lindblad dynamics. This new quantum simulation approach provides the set of the expectation values via single-qubit measurements in the mixed-state quantum process and remarkably enables to compute  $\dot{C}(t)$  without requiring the information of the correlation function  $C(t)$  in the open quantum dynamical system.

We first examined the dynamics of a spin-1/2 open quantum system. The simulations were performed in analytical, numerical, and experimental methods. In particular, the experimental transition rate curve from the IBMQ device is notably matched with the ideal quantum simulation. We further explored a chemistry-motivated CL model in a 1D double-well potential. In this case, we performed quantum numerical simulations with 16 qubits and the results of  $\dot{C}(t)$  successfully describe the detailed features of the quantum transition in its non-equilibrium dynamics. The quantum numerical outcomes for  $C(t)$  and  $\dot{C}(t)$  are compared with the results from ideal direct numerical integrations, and both demonstrate good agreement with the aid of many iterations of an ancillary qubit in the modular Lindblad evolution gate. Moreover, the modular circuits, specifically the Lindblad evolution gate, could benefit from recent advances. For example, a recently proposed variational and amplitude amplification methods for Lindblad evolution circuits may offer improved scaling properties [56, 57].

While modern numerics demands substantial computational resources and time for large-dimensional quantum problems, our proposed quantum simulation approach could achieve comparable results on the reliable NISQ devices. One promising application is to extend the CL model in 2D and 3D complex potentials tailored to address

challenges in industrial quantum chemistry (e.g., quantum hydrogen diffusion in metals [58]). For example, if each coordinate requires 128 grid points implying a 7-qubit system, the 3D CL model would necessitate storing and manipulating  $2^{21} \times 2^{21}$  matrices to compute its dynamical features at each time  $t$ . This computational burden would push the limits of memory and operational capacity even with the promising modern numerical methods. In contrast, on quantum hardware, this task would require 64 qubits based on Fig. 2 (or 43 qubits from Fig. 5) to evaluate the correlation function and/or the transition rate by single-qubit measurements since 21 qubits suffice for representing the 3D system density matrix. In addition, the exploration of simulating the dynamics of non-Markovian master equations could be feasible with this mixed-state quantum simulation approach [56]. Therefore, the advances in reliable quantum hardware hold the potential to overcome state-of-the-art computational capacity for large open quantum system simulations and to achieve practical quantum advantages across diverse fields of industrial importance, including quantum chemistry, and materials science in the future.

## Methods

### Qubits, gates and stationary states

A quantum bit (qubit) can be represented as a  $2 \times 1$  column vector and expressed as a linear combination of the computational basis states. The basis states are defined as

$$|0\rangle = \begin{pmatrix} 1 \\ 0 \end{pmatrix}, \quad \text{and} \quad |1\rangle = \begin{pmatrix} 0 \\ 1 \end{pmatrix}. \quad (29)$$

The control qubit in the quantum circuit of Fig. 2 starts from the state  $|+\rangle = (|0\rangle + |1\rangle)/\sqrt{2}$ . We use several single-qubit gates including Pauli operators

$$\hat{\sigma}_x = \begin{pmatrix} 0 & 1 \\ 1 & 0 \end{pmatrix}, \quad \hat{\sigma}_y = \begin{pmatrix} 0 & -i \\ i & 0 \end{pmatrix} \quad \text{and} \quad \hat{\sigma}_z = \begin{pmatrix} 1 & 0 \\ 0 & -1 \end{pmatrix}, \quad (30)$$

and the Hadamard gate  $\hat{H}_d \equiv (\hat{\sigma}_x + \hat{\sigma}_z)/\sqrt{2}$ .

In addition, the stationary state  $\hat{\rho}_{eq}$  of the open spin-1/2 system is given by  $\hat{\rho}_{eq} = (|0\rangle\langle 0| + |1\rangle\langle 1|)/2$ , which is an even statistical mixture of  $|0\rangle$  and  $|1\rangle$ . For the CL model, when the average thermal energy  $k_B T$  is larger than the ground state energy of the bare Hamiltonian

$$\hat{H}_0 = \frac{\hat{P}^2}{2m} + \hat{V}(x), \quad (31)$$

the stationary state is approximately given in the quantum Gibbs state [46]

$$\hat{\rho}_{eq} = \frac{e^{-\hat{H}_0/(k_B T)}}{\text{Tr}(e^{-\hat{H}_0/(k_B T)})}. \quad (32)$$

The preparation of the quantum Gibbs state on a quantum computer is an active research area and several quantum algorithms have been developed in [59–61].

## Modular Heisenberg-Lindblad evolution circuit

Here, we describe a detailed method for the modular quantum circuit for the Heisenberg-Lindblad time evolution. This scheme is inspired by the Schrödinger-Lindblad evolution algorithm introduced in [22], and essentially represents a time reversal of the circuit. The Heisenberg-Lindblad approach involves discretising time into  $N$  segments and performing the first-order integration of the dynamics. An ancillary qudit of  $d + 1$  bases is initially prepared in the fully mixed state

$$\hat{\rho}_A = \frac{1}{d+1} \left( \sum_{j=0}^d |j_{d+1}\rangle \langle j_{d+1}| \right), \quad (33)$$

where  $d$  indicates the number of Lindblad operators.

In Fig. 9, the quantum observable  $\hat{\theta}_n$  undergoes the joint unitary evolution  $e^{-i\hat{J}\sqrt{\delta}}$  with  $\hat{\rho}_A$  under the pseudo-Hamiltonian

$$\hat{J} = \begin{pmatrix} 0 & \hat{L}_1^\dagger & \cdots & \hat{L}_d^\dagger \\ \hat{L}_1 & \ddots & & 0 \\ \vdots & & \ddots & \vdots \\ \hat{L}_d & 0 & \cdots & 0 \end{pmatrix} \quad (34)$$

for a period of  $\sqrt{\delta}$ , where the time step duration is  $\delta = t_0/N$  for fixed  $t_0$ . Then, when the operation of  $e^{i\hat{H}\delta}$  is applied on the channel of  $\hat{\theta}_n$  with measurement outcome of  $|0_{d+1}\rangle$  in the channel of  $\hat{\rho}_A$ , the time evolution of  $\hat{\theta}_n$  is given by

$$\hat{\theta}_{n+1} = \hat{\theta}_n + i[\hat{H}, \hat{\theta}_n]\delta + \sum_{k=1}^d \left( \hat{L}_k^\dagger \hat{\theta}_n \hat{L}_k - \frac{1}{2} \{ \hat{\theta}_n, \hat{L}_k^\dagger \hat{L}_k \} \right) \delta + O(\delta^{3/2}). \quad (35)$$

Taking this output state and feeding it back into the same circuit for  $N$  cycles, we obtain the time-evolved observable  $\hat{\theta}(t_0)$  with the accuracy of the approximation increasing with  $N$  for a given time period  $t_0$ .

It is noteworthy that the shorter time duration  $\delta$  creates a more ideal  $\hat{\theta}_B(t)$  and implies a larger number of time steps  $N$ . One can perform the quantum circuit with the fixed  $\delta$  at different  $t_0$ , and it suggests that we need to linearly change the number

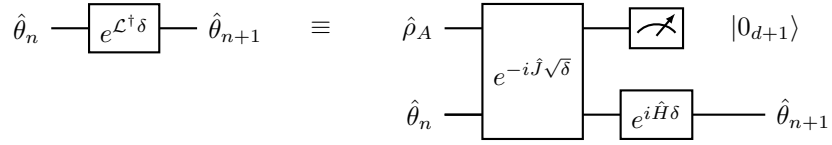


**Fig. 9:** It shows a modular Heisenberg-Lindblad quantum circuit. The success of each cycle is conditional on the measurement outcome of  $|0_{d+1}\rangle$ .



of time step  $N$  at each time  $t_0$  to create  $\hat{\theta}_B(t_0)$  since  $\delta = t_0/N$ . For example, for fixed  $\delta = 1/25$ , we require 25 iterations of the modular circuit for  $t_0 = 1$ , 50 iterations for  $t_0 = 2$ , and so on. Alternatively, we used a fixed  $N$  in the modular evolution circuit and have a more accurate evolved operator  $\hat{\theta}_B(t_0)$  for smaller  $t_0$ . Thus, to create more accurate evolved operator  $\hat{\theta}_B(t_0)$  for large  $t_0$ , we inevitably need either many iterations or many ancillary qudits in the modular evolution circuit as described in the CL model. The precise  $\hat{\theta}_B(t)$  for large  $t$  will request the exponential cost for the success probability of  $P_s \approx 1/(d+1)^N$  with  $d$  Lindblad operators. We could use the extrapolation method with results from different  $N$  as shown in the relative error plots. The success probability issue may be practically mitigated by utilising the repeat-until-success protocol in the modular evolution gate  $e^{\mathcal{L}^\dagger t}$ , and this allows all other qubits to be prepared after the successful preparation of  $\hat{\theta}_B(t)$  at  $\hat{\Phi}_1$  in Fig. 2. In addition, this scaling issue may be improved by high-order Lindblad evolution schemes and amplitude amplification methods in [56, 57].

## Analytical and numerical methods for the spin-1/2 model

As a simple physical example, we consider the single spin-1/2 system located in the magnetic field along the  $y$ -axis, which causes spin precessing around the  $y$ -axis with dephasing in the  $z$ -direction as the environment effect to the spin system. In this system,  $\hat{\theta}_B(t)$  is analytically expressed in the Pauli operators

$$\hat{\theta}_B(t) = \frac{1}{2} \mathbb{I} + \sum_{k=x,y,z} c_k(t) \hat{\sigma}_k, \quad (36)$$

and with the initial observables  $\hat{\theta}_A = |0\rangle\langle 0|$  and  $\hat{\theta}_B(0) = |1\rangle\langle 1|$  at  $t = 0$ . If we insert

$$c_x(t) = e^{-\frac{\gamma}{\hbar}t} \frac{\mu}{\hbar\omega} \sinh(\omega t), \quad (37)$$

$$c_z(t) = -\frac{e^{-\frac{\gamma}{\hbar}t}}{2} \left( \cosh(\omega t) + \frac{\gamma}{\hbar\omega} \sinh(\omega t) \right), \quad (38)$$

, and  $c_y(t) = 0$  with  $\omega = \sqrt{(\gamma^2 - 4\mu^2)/\hbar^2}$  into Eq. (36), we obtain the analytical solutions of  $C(t)$  and  $\dot{C}(t)$  in Eqs. (19) and (20).

In the quantum numerical simulation of the Heisenberg-Lindblad evolution, we apply the conditional iteration method to build the density matrix  $\hat{\theta}_B(t)$  using QuTiP [52]. For example, an ancillary qubit was employed, with 25 sequential iterations conducted for each time  $t$ . In Fig. 4, we varied the number of successful iterations from 3 to 200 at fixed evolution time  $t = 1$ .

## Experimental methods on the IBMQ machine

The experimental quantum circuit in Fig. 10 is represented with three ancillary qubits ( $A_1 - A_3$ ) and shows how to obtain the correlation function and the transition rate with the control qubit measurements ( $q_c$ ) run on the *ibm.brisbane* quantum device. To simulate the transition rate  $\dot{C}(t)$  in the spin-1/2 example, it is sufficient to compute

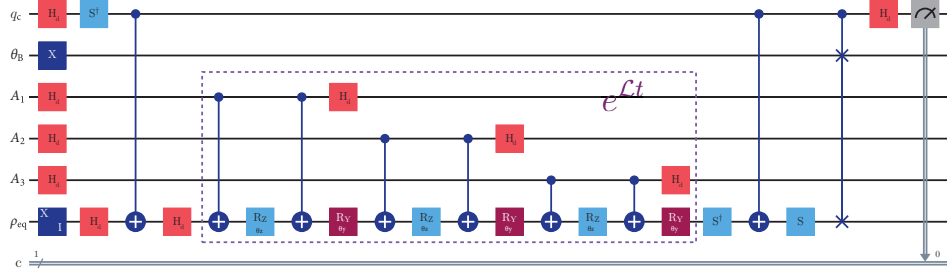


**Fig. 10:** The six-qubit IBMQ quantum circuit for calculating  $\mathcal{E}_{\hat{H}_1}(t)$ . The three ancillary qubits  $A_1 - A_3$  are used for the Schrödinger-Lindblad evolution gate  $e^{\mathcal{L}t}$  in the dashed box. The first gate at the bottom shows either  $\hat{\sigma}_x$ -gate or the identity  $\mathbb{I}$  to create the  $\hat{\rho}_{eq} = |0\rangle\langle 0|$  or  $|1\rangle\langle 1|$  probabilistically.

one of the expectation values, named  $\mathcal{E}_{\hat{H}_1}$ , without the controlled- $\hat{N}$  gate in Fig. 5. Fig. 10 actually combines two quantum circuits: one with a  $\hat{\sigma}_x$ -gate and the other with the identity gate in  $\hat{\rho}_{eq}$  (the bottom qubit) to create the fully mixed state in Eq. (18). The first CNOT gate is involved in implementing the controlled- $\hat{\theta}_A$  gate and the next six CNOT gates in the dashed box are used for the Schrödinger-Lindblad evolution gate with the three iterations of the ancillary qubit. The last CNOT gate is used for the controlled- $\hat{M}$  gate. For each set of the quantum simulations, we measure the state of the controlled qubit in  $\hat{\sigma}_z$  at each time  $t \in \{0, 0.2, 0.4, 0.6, 0.8, 1\}$  to obtain ten sets of 20,000 shots for  $C(t)$  and five sets of 20,000 shots for  $\hat{C}(t)$ . Then, we compute the average quantities of each set values of  $C(t)$  and  $\hat{C}(t)$  with the standard error. The details of the analytic justification of the expectation values and the tables of measurement data sets are provided in the Supplementary Information.

## References

- [1] Guo, S., Sun, J., Qian, H., Gong, M., *et al.*: Experimental quantum computational chemistry with optimized unitary coupled cluster ansatz. *Nature Physics* **20**, 1–7 (2024)
- [2] Chan, H.H.S., Meister, R., Jones, T., Tew, D.P., Benjamin, S.C.: Grid-based methods for chemistry simulations on a quantum computer. *Science Advances* **9**(9), 7484 (2023)
- [3] Su, Y., Berry, D.W., Wiebe, N., Rubin, N., Babbush, R.: Fault-tolerant quantum simulations of chemistry in first quantization. *PRX Quantum* **2**(4), 040332 (2021)
- [4] Bauer, B., Bravyi, S., Motta, M., Chan, G.K.-L.: Quantum algorithms for quantum chemistry and quantum materials science. *Chemical Reviews* **120**(22),

12685–12717 (2020)

- [5] Busnaina, J.H., Shi, Z., McDonald, A., Dubyna, D., Nsanzineza, I., Hung, J.S., Chang, C.S., Clerk, A.A., Wilson, C.M.: Quantum simulation of the bosonic Kitaev chain. *Nature Communications* **15**(1), 3065 (2024)
- [6] Chertkov, E., Cheng, Z., Potter, A.C., *et al.*: Characterizing a non-equilibrium phase transition on a quantum computer. *Nature physics* **19**, 1799–1804 (2023)
- [7] Cygorek, M., Cosacchi, M., Vagov, A., Axt, V.M., Lovett, B.W., Keeling, J., Gauger, E.M.: Simulation of open quantum systems by automated compression of arbitrary environments. *Nature Physics* **18**(6), 662–668 (2022)
- [8] Bauer, C.W., Davoudi, Z., Balantekin, A.B., Bhattacharya, T., Carena, M., De Jong, W.A., Draper, P., El-Khadra, A., Gemelke, N., Hanada, M., *et al.*: Quantum simulation for high-energy physics. *PRX quantum* **4**(2), 027001 (2023)
- [9] Davoudi, Z., Linke, N.M., Pagano, G.: Toward simulating quantum field theories with controlled phonon-ion dynamics: A hybrid analog-digital approach. *Physical Review Research* **3**(4), 043072 (2021)
- [10] Schäfer, F., Fukuhara, T., Sugawa, S., Takasu, Y., Takahashi, Y.: Tools for quantum simulation with ultracold atoms in optical lattices. *Nature Reviews Physics* **2**(8), 411–425 (2020)
- [11] Antonini, S., Swingle, B.: Cosmology at the end of the world. *Nature Physics* **16**(8), 881–886 (2020)
- [12] Barata, J., Mukherjee, S.: Probing celestial energy and charge correlations through real-time quantum simulations: Insights from the Schwinger model. *arXiv preprint arXiv:2409.13816* (2024)
- [13] Viermann, C., Sparn, M., Liebster, N., Hans, M., Kath, E., Parra-López, Á., Tolosa-Simeón, M., Sánchez-Kuntz, N., Haas, T., Strobel, H., *et al.*: Quantum field simulator for dynamics in curved spacetime. *nature* **611**(7935), 260–264 (2022)
- [14] Feynman, R.P.: Simulating physics with computers. *International Journal of Theoretical Physics* **21**(6) (1982)
- [15] Preskill, J.: Quantum computing in the NISQ era and beyond. *Quantum* **2**, 79 (2018)
- [16] Arute, F., Arya, K., Babbush, R., Bacon, D., Bardin, J.C., Barends, R., Biswas, R., Boixo, S., Brandao, F.G., Buell, D.A., *et al.*: Quantum supremacy using a programmable superconducting processor. *Nature* **574**, 505–510 (2019)
- [17] Chen, S., Cotler, J., Huang, H.-Y., Li, J.: The complexity of nisq. *Nature*

- [18] Samach, G.O., Greene, A., Borregaard, J., Christandl, M., Barreto, J., Kim, D.K., McNally, C.M., Melville, A., Niedzielski, B.M., Sung, Y., *et al.*: Lindblad tomography of a superconducting quantum processor. *Physical Review Applied* **18**(6), 064056 (2022)
- [19] David, I.J., Sinayskiy, I., Petruccione, F.: Digital simulation of single qubit Markovian open quantum systems: a tutorial. *Quanta*; 12: 131-163 (2023)
- [20] Liu, H.-Y., Lin, X., Chen, Z.-Y., Xue, C., Sun, T.-P., Li, Q.-S., Zhuang, X.-N., Wang, Y.-J., Wu, Y.-C., Gong, M., *et al.*: Simulation of open quantum systems on universal quantum computers. *arXiv preprint arXiv:2405.20712* (2024)
- [21] Guimarães, J.D., Ruiz-Molero, A., Lim, J., Vasilevskiy, M.I., Huelga, S.F., Plenio, M.B.: Optimized noise-assisted simulation of the Lindblad equation with time-dependent coefficients on a noisy quantum processor. *Physical Review A* **109**(5), 052224 (2024)
- [22] Cleve, R., Wang, C.: Efficient quantum algorithms for simulating Lindblad evolution. *arXiv preprint arXiv:1612.09512* (2016)
- [23] Joo, J., Spiller, T.P.: Commutation simulator for open quantum dynamics. *New Journal of Physics* **25**(8), 083041 (2023)
- [24] Campaioli, F., Cole, J.H., Hapuarachchi, H.: Quantum master equations: Tips and tricks for quantum optics, quantum computing, and beyond. *PRX Quantum* **5**(2), 020202 (2024)
- [25] Christ, A., Laiho, K., Eckstein, A., Cassemiro, K.N., Silberhorn, C.: Probing multimode squeezing with correlation functions. *New Journal of Physics* **13**(3), 033027 (2011)
- [26] Islam, R., Edwards, E., Kim, K., Korenblit, S., Noh, C., Carmichael, H., Lin, G.-D., Duan, L.-M., Joseph Wang, C.-C., Freericks, J., *et al.*: Onset of a quantum phase transition with a trapped ion quantum simulator. *Nature communications* **2**(1), 377 (2011)
- [27] Du, L.-H., You, J., Tian, L.: Superconducting circuit probe for analog quantum simulators. *Physical Review A* **92**(1), 012330 (2015)
- [28] Hsieh, C.-Y., Kapral, R.: Correlation functions in open quantum-classical systems. *Entropy* **16**(1), 200-220 (2013)
- [29] Braumüller, J., Karamlou, A.H., Yanay, Y., Kannan, B., Kim, D., Kjaergaard, M., Melville, A., Niedzielski, B.M., Sung, Y., Vepsäläinen, A., *et al.*: Probing quantum information propagation with out-of-time-ordered correlators. *Nature*

- Physics **18**(2), 172–178 (2022)
- [30] Bose, A.: Quantum correlation functions through tensor network path integral. *The Journal of Chemical Physics* **159**(21) (2023)
- [31] Alhambra, Á.M., Riddell, J., García-Pintos, L.P.: Time evolution of correlation functions in quantum many-body systems. *Physical Review Letters* **124**(11), 110605 (2020)
- [32] Kökcü, E., Labib, H.A., Freericks, J., Kemper, A.: A linear response framework for quantum simulation of bosonic and fermionic correlation functions. *Nature Communications* **15**(1), 3881 (2024)
- [33] Haack, C., Kamar, N.A., Paz, D., Maghrebi, M., Gong, Z.: Probing non-equilibrium dissipative phase transitions with trapped-ion quantum simulators. arXiv preprint arXiv:2311.06199 (2023)
- [34] Marcolongo, A., Umari, P., Baroni, S.: Microscopic theory and quantum simulation of atomic heat transport. *Nature Physics* **12**(1), 80–84 (2016)
- [35] Voth, G.A., Chandler, D., Miller, W.H.: Time correlation function and path integral analysis of quantum rate constants. *The Journal of Physical Chemistry* **93**(19), 7009–7015 (1989)
- [36] Hele, T.J.: Thermal quantum time-correlation functions from classical-like dynamics. *Molecular Physics* **115**(13), 1435–1462 (2017)
- [37] Zwanzig, R.: Time-correlation functions and transport coefficients in statistical mechanics. *Annual Review of Physical Chemistry* **16**(1), 67–102 (1965)
- [38] Onsager, L.: Reciprocal relations in irreversible processes. ii. *Physical review* **38**(12), 2265 (1931)
- [39] Chandler, D.: *Introduction to Modern Statistical Mechanics*. Oxford University Press, Oxford (1987)
- [40] Berezhkovskii, A.M., Szabo, A.: Population fluctuations at equilibrium and Kramers’ rate of diffusive barrier crossing. *The Journal of Physical Chemistry B* **127**(22), 5084–5088 (2023)
- [41] Lax, M.: Formal theory of quantum fluctuations from a driven state. *Physical Review* **129**(5), 2342 (1963)
- [42] Gardiner, C., Zoller, P.: *Quantum Noise: a Handbook of Markovian and Non-Markovian Quantum Stochastic Methods with Applications to Quantum Optics*. Springer, Heidelberg (2004)
- [43] Khan, S., Agarwalla, B.K., Jain, S.: Quantum regression theorem for multi-time

- correlators: A detailed analysis in the Heisenberg picture. *Physical Review A* **106**(2), 022214 (2022)
- [44] Smirne, A., Tamascelli, D., Lim, J., Plenio, M.B., Huelga, S.F.: Non-perturbative treatment of open-system multi-time expectation values in Gaussian bosonic environments. *Open Systems & Information Dynamics* **29**(04), 2250019 (2022)
- [45] Caldeira, A.O., Leggett, A.J.: Path integral approach to quantum brownian motion. *Physica A: Statistical mechanics and its Applications* **121**(3), 587–616 (1983)
- [46] Breuer, H.-P., Petruccione, F.: *The Theory of Open Quantum Systems*. Oxford University Press, Oxford (2002)
- [47] Gorini, V., Kossakowski, A., Sudarshan, E.C.G.: Completely positive dynamical semigroups of n-level systems. *Journal of Mathematical Physics* **17**(5), 821–825 (1976)
- [48] Lindblad, G.: On the generators of quantum dynamical semigroups. *Communications in Mathematical Physics* **48**(2), 119–130 (1976)
- [49] McCauley, G., Cruikshank, B., Bondar, D.I., Jacobs, K.: Accurate Lindblad-form master equation for weakly damped quantum systems across all regimes. *npj Quantum Information* **6**(1), 74 (2020)
- [50] Manzano, D.: A short introduction to the Lindblad master equation. *AIP advances* **10**(2) (2020)
- [51] Craig, I.R., Manolopoulos, D.E.: Quantum statistics and classical mechanics: Real time correlation functions from ring polymer molecular dynamics. *The Journal of chemical physics* **121**(8), 3368–3373 (2004)
- [52] Johansson, J.R., Nation, P.D., Nori, F.: Qutip: An open-source python framework for the dynamics of open quantum systems. *Computer Physics Communications* **183**(8), 1760–1772 (2012)
- [53] IBM Quantum, <https://quantum-computing.ibm.com>.
- [54] Wille, R., Van Meter, R., Naveh, Y.: IBM’s qiskit tool chain: Working with and developing for real quantum computers. In: *2019 Design, Automation & Test in Europe Conference & Exhibition*, pp. 1234–1240 (2019). IEEE
- [55] Joo, J., Moon, H.: Quantum variational PDE solver with machine learning. arXiv preprint arXiv:2109.09216 (2021)
- [56] Li, X., Wang, C.: Simulating Markovian open quantum systems using higher-order series expansion. In: *50th International Colloquium on Automata, Languages, and Programming, ICALP 2023*, p. 87 (2023). Schloss Dagstuhl-Leibniz-Zentrum

fur Informatik GmbH, Dagstuhl Publishing

- [57] Childs, A.M., Li, T.: Efficient simulation of sparse Markovian quantum dynamics. *Quantum Information & Computation* **17**(11-12), 901–947 (2017)
- [58] Beachem, C.: A new model for hydrogen-assisted cracking (hydrogen “embrittlement”). *Metallurgical and Materials Transactions B* **3**(2), 441–455 (1972)
- [59] Rall, P., Wang, C., Wocjan, P.: Thermal state preparation via rounding promises. *Quantum* **7**, 1132 (2023)
- [60] Gu, A., Cincio, L., Coles, P.J.: Practical Hamiltonian learning with unitary dynamics and Gibbs states. *Nature Communications* **15**(1), 312 (2024)
- [61] Consiglio, M., Settino, J., Giordano, A., Mastroianni, C., Plastina, F., Lorenzo, S., Maniscalco, S., Goold, J., Apollaro, T.J.: Variational gibbs state preparation on noisy intermediate-scale quantum devices. *Physical Review A* **110**(1), 012445 (2024)
- [62] Schlosshauer, M.A.: *Decoherence: and the Quantum-to-classical Transition*. Springer, Heidelberg (2007)
- [63] Gorini, V., Kossakowski, A., Sudarshan, E.C.G.: Completely positive dynamical semigroups of N-level systems. *Journal of Mathematical Physics* **17**(5), 821–825 (1976)
- [64] Kabernik, O.: Transition to the classical regime in quantum mechanics on a lattice and implications of discontinuous space. *Physical Review A* **104**(5), 052206 (2021)

**Acknowledgments:** We acknowledge the support from the Institute for Information & communications Technology Promotion (IITP) grant funded by the Korea government (MSIP) (No. 2019-000003, Research and Development of Core technologies for Programming, Running, Implementing and Validating of Fault-Tolerant Quantum Computing System). J. B. and K. B. thank to the support of the Ministry of Trade, Industry, and Energy (MOTIE), Korea, under the project “Industrial Technology Infrastructure Program” (RS-2024-00466693) and the National Research Foundation of Korea (NRF-2023M3K5A1094813 and RS-2023-00281456). We also acknowledge the utilization of IBM quantum services in conducting this work. The views expressed are those of the authors and do not reflect the official policy or position of IBM or the IBM Quantum team.

**Author Contributions:** J. J. and R. C. initiated the research and conducted the research. All authors prepared and revised the manuscript and contributed to experiments and discussions.

**Competing interests:** The authors declare no competing financial interests.

**Data Availability:** The data that support the findings of this study are presented in the article and the Supplementary Information, and are available from the corresponding authors upon reasonable request. Source data is provided with this paper.

**Additional Information:** Correspondence and requests for materials should be addressed to J. J. (jaewoo.joo@port.ac.uk).

## Supplementary Information

### Transition rate theory

In this section, we first review the classical transition rate theory based on [39], before introducing an analogous quantum formulation in Lindblad dynamics. To define a transition between the “states”, we first identify metastable subspaces  $A$  and  $B$  within the phase space of the system. We use characteristic functions to define the state functions for regions  $A$  and  $B$  as follows:

$$\theta_A(x) = \begin{cases} 1, & \text{if } x \in A, \\ 0, & \text{if } x \notin A, \end{cases} \quad \text{and} \quad \theta_B(x) = \begin{cases} 1, & \text{if } x \in B, \\ 0, & \text{if } x \notin B. \end{cases} \quad (39)$$

If we consider the case of many non-interacting particles at equilibrium, the populations of states  $A$  and  $B$  fluctuate due to transitions between these states. Consequently, the transition dynamics can be described by the temporal correlation of the populations of states from  $x_0$  to  $x_t$  as follows:

$$C(t) = \frac{\langle \theta_A(x_0) \theta_B(x_t) \rangle_{eq}}{\langle \theta_A(x_0) \rangle_{eq}} \quad (40)$$

In this expression,  $\langle \cdot \rangle_{eq}$  represents the average over the equilibrium distribution of the initial state.

The correlation function  $C(t)$  implies the conditional probability of observing the system in state  $B$  at time  $t$  assuming that it started from state  $A$  at  $t = 0$  as shown in Fig. 1 in the main text. By the linear response theory [38–40], the rate of equilibrium fluctuations from  $A$  to  $B$  is given by the rate of relaxation as the system recovers from a non-equilibrium condition in which only state  $A$  is initially occupied. For brief intervals,  $C(t)$  reflects the microscopic movements within the transition state area, linked over the molecular timescale  $t_{mol}$  [39], which represents the time required to traverse the barrier separating the stable regions and settle into one of the states. However, on timescales longer than  $t_{mol}$ , a two-state kinetic model provides a good description of the transition dynamics. In this model, the transitions are rare compared to the time spent in the metastable states. The dynamical model can be represented



as follows:

$$\frac{d}{dt} \langle \theta_A \rangle_{ne}(t) = -k_{AB} \langle \theta_A \rangle_{ne}(t) + k_{BA} \langle \theta_B \rangle_{ne}(t), \quad (41)$$

$$\frac{d}{dt} \langle \theta_B \rangle_{ne}(t) = k_{AB} \langle \theta_A \rangle_{ne}(t) - k_{BA} \langle \theta_B \rangle_{ne}(t). \quad (42)$$

The expectation values are denoted as the time-dependent non-equilibrium phase-space probability density and the solutions are

$$\langle \theta_A \rangle_{ne}(t) = \frac{k_{BA} + k_{AB} e^{-(k_{AB}+k_{BA})t}}{k_{AB} + k_{BA}}, \quad (43)$$

$$\langle \theta_B \rangle_{ne}(t) = \frac{k_{AB} (1 - e^{-(k_{AB}+k_{BA})t})}{k_{AB} + k_{BA}}, \quad (44)$$

which satisfy the kinetic equations with the initial conditions at  $t = 0$

$$\langle \theta_A \rangle_{ne}(0) = 1 \quad \text{and} \quad \langle \theta_B \rangle_{ne}(0) = 0. \quad (45)$$

After an initial transient time  $t_{mol}$ , the population dynamics of the double well system are well described by a two-state kinetic model. The initial conditions are equivalent to the definition of  $C(t)$  as the conditional probability of observing the system in state  $B$  at time  $t$  such as

$$C(t) = \langle \theta_B \rangle_{ne}(t). \quad (46)$$

Expanding to Eq. (44) for short times (the first order in  $t$ ) in the linear response domain, the correlation function is

$$C(t) \approx k_{AB}t. \quad (47)$$

Therefore, if we start the system in the state  $A$ , the gradient of  $C(t)$  represents the constant rate  $\dot{C}(t) \approx k_{AB}$ .

The classical concepts extend to quantum systems by replacing the classical characteristic functions with analogous projection operators:

$$\hat{\theta}_A = \int_{x \in A} dx |x\rangle \langle x| \quad \text{and} \quad \hat{\theta}_B = \int_{x \in B} dx |x\rangle \langle x|, \quad (48)$$

The quantum correlation function derivative is thus given by

$$\dot{C}_C(t) \equiv \frac{\langle \hat{\theta}_A(0) \dot{\hat{\theta}}_B(t) \rangle_{eq}}{\langle \hat{\theta}_A(0) \rangle_{eq}}. \quad (49)$$

and is complex-valued. The real part of Eq. (3) is identified as the rate while the imaginary component contains phase information [51]. Since the projectors are Hermitian, the rate component of the correlation function is given by the anti-commutator

expectation value

$$\dot{C}(t) \equiv \frac{\langle \{\hat{\theta}_A(0), \dot{\hat{\theta}}_B(t)\} \rangle_{eq}}{2 \langle \hat{\theta}_A(0) \rangle_{eq}}. \quad (50)$$

More explicitly the above may be written in the form

$$\dot{C}(t) = \frac{\text{Tr} \left( \hat{\rho}_{eq} \left\{ \hat{\theta}_A, \mathcal{L}^\dagger \left( e^{\mathcal{L}^\dagger t} (\hat{\theta}_B) \right) \right\} \right)}{2 \text{Tr} \left( \hat{\rho}_{eq} \hat{\theta}_A \right)}. \quad (51)$$

where  $\hat{\rho}_{eq}$  is the equilibrium state of the Lindblad dynamics and the time evolution of the observables is governed by the Heisenberg picture Lindblad evolution equation:

$$\frac{d}{dt} \hat{\theta}(t) = \mathcal{L}^\dagger \left( \hat{\theta}(t) \right) = \frac{i}{\hbar} [\hat{H}, \hat{\theta}(t)] + \frac{1}{\hbar} \sum_k \left( \hat{L}_k^\dagger \hat{\theta}(t) \hat{L}_k - \frac{1}{2} \{ \hat{\theta}(t), \hat{L}_k^\dagger \hat{L}_k \} \right). \quad (52)$$

By expanding the commutators and rearranging the terms in Eq. (51), we can reformulate the transition rate in terms of the Schrödinger picture dynamics as follows

$$\dot{C}(t) = \frac{\text{Tr} \left( \hat{\theta}_B \mathcal{L} \left( e^{\mathcal{L}t} \left( \left\{ \hat{\rho}_{eq}, \hat{\theta}_A \right\} \right) \right) \right)}{2 \text{Tr} \left( \hat{\rho}_{eq} \hat{\theta}_A \right)}. \quad (53)$$

with the standard form of the Lindblad equation:

$$\frac{d}{dt} \hat{\rho}(t) = \mathcal{L}(\hat{\rho}(t)) = -\frac{i}{\hbar} [\hat{H}, \hat{\rho}(t)] + \frac{1}{\hbar} \sum_k \left( \hat{L}_k \hat{\rho}(t) \hat{L}_k^\dagger - \frac{1}{2} \{ \hat{\rho}(t), \hat{L}_k^\dagger \hat{L}_k \} \right). \quad (54)$$

## Correlation function derivative circuits

### Heisenberg picture derivative circuit

We provide the mathematical details for how the expectation value corresponding to a  $\hat{\sigma}_z$  measurement on the control qubit at  $\hat{\Phi}_4$  is computed in the Heisenberg picture derivative circuit such as

$$\text{Tr} \left( \hat{\sigma}_z^c \hat{\Phi}_4 \right) = \frac{1}{2} \left\langle e^{-i\chi} \{ \hat{\theta}_A, \hat{M}^\dagger \hat{\theta}_B(t) \hat{N}^\dagger \} + e^{i\chi} \{ \hat{\theta}_A, \hat{N} \hat{\theta}_B(t) \hat{M} \} \right\rangle_{eq}, \quad (55)$$

here the superscript  $c$  in  $\hat{\sigma}_z^c$  indicates a  $\hat{\sigma}_z$  operator on the control qubit and identity operators on all other channels. We denote the total density operator at stage  $n$  as  $\hat{\Phi}_n$ . Our initial circuit input is the state

$$\hat{\Phi}_0 = |+\rangle \langle +| \otimes \hat{\theta}_B \otimes \hat{\theta}_A \otimes \hat{\rho}_{eq}, \quad (56)$$

with the control qubit in the  $|+\rangle$  state, and the projection operators  $\hat{\theta}_A$  and  $\hat{\theta}_B$  defining stable states, along with  $\hat{\rho}_{eq}$  representing the equilibrium state. In the next stage,

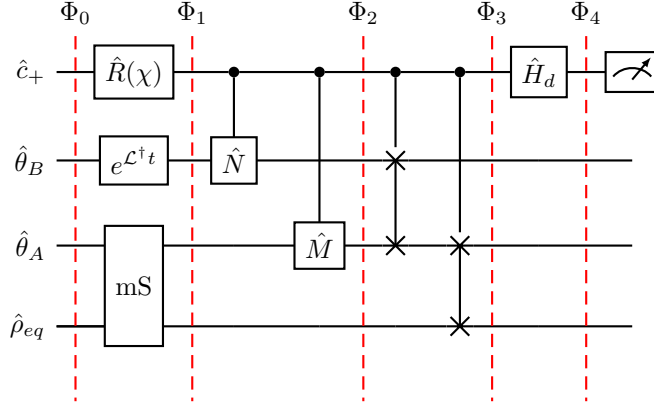


**Fig. 11:** Heisenberg picture correlation function derivative circuit.

we apply a phase-shifted rotation- $z$  operator to the control qubit such as  $\hat{R}(\chi) = e^{-i\chi(\hat{\sigma}_z - 1)/2}$ . For the  $\hat{\theta}_B$  channel, we perform the time evolution of the observable  $\hat{\theta}_B(0)$  up to time  $t$  to create  $\hat{\theta}_B(t)$ . For the other two channels, we implement a mixed swap gate that executes the following operation:

$$\hat{\theta}_A \otimes \hat{\rho}_{eq} \rightarrow \frac{1}{2}(\hat{\theta}_A \otimes \hat{\rho}_{eq} + \hat{\rho}_{eq} \otimes \hat{\theta}_A). \quad (57)$$

This mixed swap operation can be implemented by stochastically swapping the third and fourth input channels as indicated in Fig. 11. The state  $\hat{\Phi}_1$  after the first stage of evolution is given by:

$$\hat{\Phi}_1 = \frac{1}{4} (|0\rangle\langle 0| + e^{-i\chi}|0\rangle\langle 1| + e^{i\chi}|1\rangle\langle 0| + |1\rangle\langle 1|) \otimes \hat{\theta}_B(t) \otimes (\hat{\theta}_A \otimes \hat{\rho}_{eq} + \hat{\rho}_{eq} \otimes \hat{\theta}_A). \quad (58)$$

The above equation includes both the original and swapped configurations of  $\hat{\theta}_A$  and  $\hat{\rho}_{eq}$ . To maintain compact notation in further derivations, we use the suffix +SW( $\hat{\theta}_A, \hat{\rho}_{eq}$ ) to signify that identical terms with swapped  $\hat{\theta}_A$  and  $\hat{\rho}_{eq}$  are added. Thus, Eq. (58) can be expressed as:

$$\hat{\Phi}_1 = \frac{1}{4} (|0\rangle\langle 0| + e^{-i\chi}|0\rangle\langle 1| + e^{i\chi}|1\rangle\langle 0| + |1\rangle\langle 1|) \otimes \hat{\theta}_B(t) \otimes \hat{\theta}_A \otimes \hat{\rho}_{eq} + \text{SW}(\hat{\theta}_A, \hat{\rho}_{eq}). \quad (59)$$

Applying the controlled unitary gates  $\hat{N}$  and  $\hat{M}$  as in Fig. 11 gives

$$\begin{aligned} \hat{\Phi}_2 = \frac{1}{4} & \left( |0\rangle\langle 0| \otimes \hat{\theta}_B(t) \otimes \hat{\theta}_A \otimes \hat{\rho}_{eq} + e^{-i\chi}|0\rangle\langle 1| \otimes \hat{\theta}_B(t)\hat{N}^\dagger \otimes \hat{\theta}_A\hat{M}^\dagger \otimes \hat{\rho}_{eq} \right. \\ & \left. + e^{i\chi}|1\rangle\langle 0| \otimes \hat{N}\hat{\theta}_B(t) \otimes \hat{M}\hat{\theta}_A \otimes \hat{\rho}_{eq} + |1\rangle\langle 1| \otimes \hat{N}\hat{\theta}_B(t)\hat{N}^\dagger \otimes \hat{M}\hat{\theta}_A\hat{M}^\dagger \otimes \hat{\rho}_{eq} \right) \\ & + \text{SW}(\hat{\theta}_A, \hat{\rho}_{eq}). \end{aligned} \quad (60)$$

Next applying the double block C-SWAP [55] gates gives

$$\begin{aligned}\hat{\Phi}_3 &= \frac{1}{4} \left( |0\rangle \langle 0| \otimes \hat{\theta}_B(t) \otimes \hat{\theta}_A \otimes \hat{\rho}_{eq} + e^{-i\chi} |0\rangle \langle 1| \otimes \left( \hat{\theta}_B(t) \hat{N}^\dagger \xleftrightarrow[\text{b1}]{\otimes} \hat{\theta}_A \hat{M}^\dagger \right) \xleftrightarrow[\text{b2}]{\otimes} \hat{\rho}_{eq} \right. \\ &+ e^{i\chi} |1\rangle \langle 0| \otimes \left( \hat{N} \hat{\theta}_B(t) \xleftrightarrow[\text{k1}]{\otimes} \hat{M} \hat{\theta}_A \right) \xleftrightarrow[\text{k2}]{\otimes} \hat{\rho}_{eq} + |1\rangle \langle 1| \otimes \hat{M} \hat{\theta}_A \hat{M}^\dagger \otimes \hat{\rho}_{eq} \otimes \hat{N} \hat{\theta}_B(t) \hat{N}^\dagger \Big) \\ &+ \text{SW}(\hat{\theta}_A, \hat{\rho}_{eq}).\end{aligned}\quad (61)$$

Finally, we write the state just before the measurement as

$$\begin{aligned}\hat{\Phi}_4 &= \frac{1}{4} \left( |+\rangle \langle +| \otimes \hat{\theta}_B(t) \otimes \hat{\theta}_A \otimes \hat{\rho}_{eq} + e^{-i\chi} |+\rangle \langle -| \otimes \left( \hat{\theta}_B(t) \hat{N}^\dagger \xleftrightarrow[\text{b1}]{\otimes} \hat{\theta}_A \hat{M}^\dagger \right) \xleftrightarrow[\text{b2}]{\otimes} \hat{\rho}_{eq} \right. \\ &+ e^{i\chi} |-\rangle \langle +| \otimes \left( \hat{N} \hat{\theta}_B(t) \xleftrightarrow[\text{k1}]{\otimes} \hat{M} \hat{\theta}_A \right) \xleftrightarrow[\text{k2}]{\otimes} \hat{\rho}_{eq} + |-\rangle \langle -| \otimes \hat{M} \hat{\theta}_A \hat{M}^\dagger \otimes \hat{\rho}_{eq} \otimes \hat{N} \hat{\theta}_B(t) \hat{N}^\dagger \Big) \\ &+ \text{SW}(\hat{\theta}_A, \hat{\rho}_{eq}).\end{aligned}\quad (62)$$

When expanding in the control qubit computational basis, we note that the non-diagonal terms, specifically  $|0\rangle \langle 1|$  and  $|1\rangle \langle 0|$ , do not contribute to the  $\hat{\sigma}_z^c$  measurement statistics. Performing the control qubit measurement we have

$$\text{Tr}(\hat{\sigma}_z^c \hat{\Phi}_4) = \frac{1}{2} \left\langle e^{-i\chi} \{ \hat{\theta}_A, \hat{M}^\dagger \hat{\theta}_B(t) \hat{N}^\dagger \} + e^{i\chi} \{ \hat{\theta}_A, \hat{N} \hat{\theta}_B(t) \hat{M} \} \right\rangle_{eq}. \quad (63)$$

By changing the phase gate parameter  $\chi$  and the controlled- $\hat{M}$  and  $-\hat{N}$  gates, we can reproduce expectation values of the terms in the Heisenberg picture Lindblad equation in Eq. (52). For the Hamiltonian terms with the anti-commutator, we have  $\chi = -\pi/2$ ,  $\hat{N} = \mathbb{I}$ , and  $\hat{M} = \hat{H}$  and thus

$$\mathcal{E}_H = \frac{2}{\hbar} \text{Tr}(\hat{\sigma}_z^c \hat{\Phi}_4) = \frac{i}{\hbar} \left\langle \{ \hat{\theta}_A, [\hat{H}, \hat{\theta}_B(t)] \} \right\rangle_{eq}. \quad (64)$$

For the jump term we have  $\chi = 0$ ,  $\hat{N} = \hat{L}^\dagger$ , and  $\hat{M} = \hat{L}$

$$\mathcal{E}_J = \frac{1}{\hbar} \text{Tr}(\hat{\sigma}_z^c \hat{\Phi}_4) = \frac{1}{\hbar} \left\langle \{ \hat{\theta}_A, \hat{L}^\dagger \hat{\theta}_B(t) \hat{L} \} \right\rangle_{eq}. \quad (65)$$

The double anti-commutator terms we have  $\chi = 0$ ,  $\hat{N} = \mathbb{I}$  and  $\hat{M} = \hat{L}^\dagger \hat{L}$

$$\mathcal{E}_{AC} = -\frac{1}{\hbar} \text{Tr}(\hat{\sigma}_z^c \hat{\Phi}_4) = -\frac{1}{2\hbar} \left\langle \{ \hat{\theta}_A, \{ \hat{\theta}_B(t), \hat{L}^\dagger \hat{L} \} \} \right\rangle_{eq}. \quad (66)$$

Finally for the denominator we have  $\chi = 0$ ,  $\hat{N} = \mathbb{I}$ ,  $\hat{M} = \mathbb{I}$  and we input  $\hat{\theta}_B = \mathbb{I}$

$$\mathcal{E}_D = \text{Tr}(\hat{\sigma}_z^c \hat{\Phi}_4) = \left\langle \hat{\theta}_A \right\rangle_{eq}. \quad (67)$$

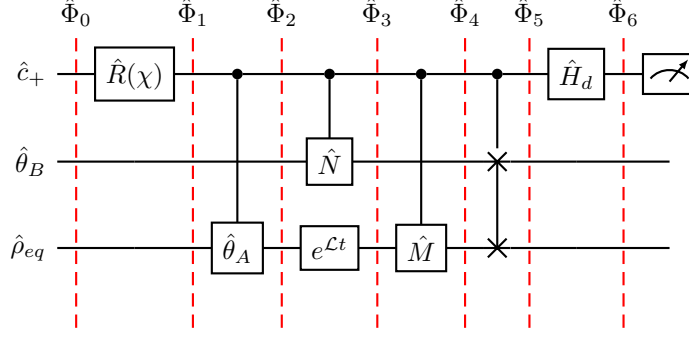


**Fig. 12:** Schrödinger picture correlation function derivative circuit.

Combining all these terms we can therefore write the correlation function derivative as

$$\dot{C}(t) = \frac{\mathcal{E}_H + \mathcal{E}_J + \mathcal{E}_{AC}}{2\mathcal{E}_D}. \quad (68)$$

### Schrödinger picture circuit

Here we provide the mathematical details for how the expectation value corresponding to a  $\hat{\sigma}_z$  measurement on the control qubit in the Schrödinger picture correlation derivative circuit given in Fig. 12 is determined

$$\text{Tr}\left(\hat{\sigma}_z^c \hat{\Phi}_6\right) = \frac{1}{2} \left( e^{-i\chi} \text{Tr}\left(\hat{\theta}_B \hat{N}^\dagger e^{\mathcal{L}t} \left(\hat{\rho}_{eq} \hat{\theta}_A\right) \hat{M}^\dagger\right) + e^{i\chi} \text{Tr}\left(\hat{\theta}_B \hat{M} e^{\mathcal{L}t} \left(\hat{\theta}_A \hat{\rho}_{eq}\right) \hat{N}\right) \right), \quad (69)$$

where the superscript  $c$  in  $\hat{\sigma}_z^c$  indicates a  $\hat{\sigma}_z$  operator on the control qubit. We denote the total density operator at stage  $n$  as  $\hat{\Phi}_n$ . Our initial circuit input is the state

$$\hat{\Phi}_0 = |+\rangle \langle +| \otimes \hat{\theta}_B \otimes \hat{\rho}_{eq}, \quad (70)$$

with the control qubit in the  $|+\rangle$  state, and the projection operator  $\hat{\theta}_B$  along with  $\hat{\rho}_{eq}$ . In the next stage, we apply a phase-shifted  $z$ -axis rotation operator to the control qubit such as  $\hat{R}(\chi) = e^{-i\chi(\hat{\sigma}_z - 1)/2}$ . The state  $\hat{\Phi}_1$  is given by

$$\hat{\Phi}_1 = \frac{1}{2} \left( |0\rangle \langle 0| + e^{-i\chi} |0\rangle \langle 1| + e^{i\chi} |1\rangle \langle 0| + |1\rangle \langle 1| \right) \otimes \hat{\theta}_B \otimes \hat{\rho}_{eq}. \quad (71)$$

After the controlled- $\hat{\theta}_A$  gate as in Fig. 12,  $\hat{\Phi}_2$  is given by

$$\hat{\Phi}_2 = \frac{1}{2} \left( |0\rangle \langle 0| \otimes \hat{\theta}_B \otimes \hat{\rho}_{eq} + e^{-i\chi} |0\rangle \langle 1| \otimes \hat{\theta}_B \otimes \hat{\rho}_{eq} \hat{\theta}_A + e^{i\chi} |1\rangle \langle 0| \otimes \hat{\theta}_B \otimes \hat{\theta}_A \hat{\rho}_{eq} + |1\rangle \langle 1| \otimes \hat{\theta}_B \otimes \hat{\theta}_A \hat{\rho}_{eq} \hat{\theta}_A \right). \quad (72)$$

Applying the controlled- $\hat{N}$  gate and the Lindblad time evolution gate  $e^{\mathcal{L}t}$  [22] in Fig. 12 results in

$$\begin{aligned} \hat{\Phi}_3 = & \frac{1}{2} \left( |0\rangle \langle 0| \otimes \hat{\theta}_B \otimes \hat{\rho}_{eq} + e^{-i\chi} |0\rangle \langle 1| \otimes \hat{\theta}_B \hat{N}^\dagger \otimes e^{\mathcal{L}t} \left( \hat{\rho}_{eq} \hat{\theta}_A \right) \right. \\ & \left. + e^{i\chi} |1\rangle \langle 0| \otimes \hat{N} \hat{\theta}_B \otimes e^{\mathcal{L}t} \left( \hat{\theta}_A \hat{\rho}_{eq} \right) + |1\rangle \langle 1| \otimes \hat{N} \hat{\theta}_B \hat{N}^\dagger \otimes e^{\mathcal{L}t} \left( \hat{\theta}_A \hat{\rho}_{eq} \hat{\theta}_A \right) \right). \end{aligned} \quad (73)$$

Subsequently, applying the controlled- $\hat{M}$  gate in Fig. 12 yields

$$\begin{aligned} \hat{\Phi}_4 = & \frac{1}{2} \left( |0\rangle \langle 0| \otimes \hat{\theta}_B \otimes \hat{\rho}_{eq} + e^{-i\chi} |0\rangle \langle 1| \otimes \hat{\theta}_B \hat{N}^\dagger \otimes e^{\mathcal{L}t} \left( \hat{\rho}_{eq} \hat{\theta}_A \right) \hat{M}^\dagger \right. \\ & \left. + e^{i\chi} |1\rangle \langle 0| \otimes \hat{N} \hat{\theta}_B \otimes \hat{M} e^{\mathcal{L}t} \left( \hat{\theta}_A \hat{\rho}_{eq} \right) + |1\rangle \langle 1| \otimes \hat{N} \hat{\theta}_B \hat{N}^\dagger \otimes \hat{M} e^{\mathcal{L}t} \left( \hat{\theta}_A \hat{\rho}_{eq} \hat{\theta}_A \right) \hat{M}^\dagger \right). \end{aligned} \quad (74)$$

After the block C-SWAP gates [55], the density operator becomes

$$\begin{aligned} \hat{\Phi}_5 = & \frac{1}{2} \left( |0\rangle \langle 0| \otimes \hat{\theta}_B \otimes \hat{\rho}_{eq} + e^{-i\chi} |0\rangle \langle 1| \otimes \hat{\theta}_B \hat{N}^\dagger \overset{\otimes}{\leftarrow} e^{\mathcal{L}t} \left( \hat{\rho}_{eq} \hat{\theta}_A \right) \hat{M}^\dagger \right. \\ & \left. + e^{i\chi} |1\rangle \langle 0| \otimes \hat{N} \hat{\theta}_B \overset{\otimes}{\leftarrow} \hat{M} e^{\mathcal{L}t} \left( \hat{\theta}_A \hat{\rho}_{eq} \right) + |1\rangle \langle 1| \otimes \hat{M} e^{\mathcal{L}t} \left( \hat{\theta}_A \hat{\rho}_{eq} \hat{\theta}_A \right) \hat{M}^\dagger \otimes \hat{N} \hat{\theta}_B \hat{N}^\dagger \right). \end{aligned} \quad (75)$$

We finally have the state after the Hadamard gate such as

$$\begin{aligned} \hat{\Phi}_6 = & \frac{1}{2} \left( |+\rangle \langle +| \otimes \hat{\theta}_B \otimes \hat{\rho}_{eq} + e^{-i\chi} |+\rangle \langle -| \otimes \hat{\theta}_B \hat{N}^\dagger \overset{\otimes}{\leftarrow} e^{\mathcal{L}t} \left( \hat{\rho}_{eq} \hat{\theta}_A \right) \hat{M}^\dagger \right. \\ & \left. + e^{i\chi} |-\rangle \langle +| \otimes \hat{N} \hat{\theta}_B \overset{\otimes}{\leftarrow} \hat{M} e^{\mathcal{L}t} \left( \hat{\theta}_A \hat{\rho}_{eq} \right) + |-\rangle \langle -| \otimes \hat{M} e^{\mathcal{L}t} \left( \hat{\theta}_A \hat{\rho}_{eq} \hat{\theta}_A \right) \hat{M}^\dagger \otimes \hat{N} \hat{\theta}_B \hat{N}^\dagger \right) \end{aligned} \quad (76)$$

After performing the measurements in the control qubit, we have the expectation value

$$\text{Tr} \left( \hat{\sigma}_z^c \hat{\Phi}_6 \right) = \frac{1}{2} \left( e^{-i\chi} \text{Tr} \left( \hat{\theta}_B \hat{N}^\dagger e^{\mathcal{L}t} \left( \hat{\rho}_{eq} \hat{\theta}_A \right) \hat{M}^\dagger \right) + e^{i\chi} \text{Tr} \left( \hat{\theta}_B \hat{M} e^{\mathcal{L}t} \left( \hat{\theta}_A \hat{\rho}_{eq} \right) \hat{N} \right) \right) \quad (77)$$

The transition rate in Eq. (53) is given by the sum of five input combinations divided by another measurement outcome corresponding to the denominator of Eq. (53). The five input combinations correspond to the different terms in the Lindblad equation Eq. (54). For the Hamiltonian contribution, we first have  $\chi = -\pi/2$ ,  $\hat{N} = \mathbb{I}$ , and

$\hat{M} = \hat{H}$  and thus

$$\mathcal{E}_{H1} = \frac{1}{\hbar} \text{Tr}(\hat{\sigma}_z^c \hat{\Phi}_6) = \frac{1}{2\hbar} \left( i \text{Tr}(\hat{\theta}_B e^{\mathcal{L}t} (\hat{\rho}_{eq} \hat{\theta}_A) \hat{H}) - i \text{Tr}(\hat{\theta}_B \hat{H} e^{\mathcal{L}t} (\hat{\theta}_A \hat{\rho}_{eq})) \right) \quad (78)$$

then we have  $\chi = \pi/2$ ,  $\hat{N} = \hat{H}$ , and  $\hat{M} = \mathbb{I}$

$$\mathcal{E}_{H2} = \frac{1}{\hbar} \text{Tr}(\hat{\sigma}_z^c \hat{\Phi}_6) = \frac{1}{2\hbar} \left( -i \text{Tr}(\hat{\theta}_B \hat{H} e^{\mathcal{L}t} (\hat{\rho}_{eq} \hat{\theta}_A)) + i \text{Tr}(\hat{\theta}_B e^{\mathcal{L}t} (\hat{\theta}_A \hat{\rho}_{eq} \hat{H})) \right) \quad (79)$$

Combining Eq. (78) and Eq. (79) we have

$$\mathcal{E}_{H1} + \mathcal{E}_{H2} = -\frac{i}{2\hbar} \text{Tr}(\hat{\theta}_B [\hat{H}, e^{\mathcal{L}t} (\{\hat{\rho}_{eq}, \hat{\theta}_A\})]). \quad (80)$$

For the jump term contribution we set  $\chi = 0$ ,  $\hat{N} = \hat{L}^\dagger$ , and  $\hat{M} = \hat{L}$

$$\mathcal{E}_J = \frac{1}{\hbar} \text{Tr}(\hat{\sigma}_z^c \hat{\Phi}_6) = \frac{1}{2\hbar} \left( \text{Tr}(\hat{\theta}_B \hat{L} e^{\mathcal{L}t} (\{\hat{\rho}_{eq}, \hat{\theta}_A\}) \hat{L}^\dagger) \right) \quad (81)$$

The anti-commutator contribution consists of two measurements first  $\chi = 0$ ,  $\hat{N} = \mathbb{I}$  and  $\hat{M} = \hat{L}^\dagger \hat{L}$

$$\mathcal{E}_{AC1} = -\frac{1}{2\hbar} \text{Tr}(\hat{\sigma}_z^c \hat{\Phi}_6) = -\frac{1}{4\hbar} \left( \text{Tr}(\hat{\theta}_B e^{\mathcal{L}t} (\hat{\rho}_{eq} \hat{\theta}_A) \hat{L}^\dagger \hat{L}) + \text{Tr}(\hat{\theta}_B \hat{L}^\dagger \hat{L} e^{\mathcal{L}t} (\hat{\theta}_A \hat{\rho}_{eq})) \right) \quad (82)$$

and next  $\chi = 0$ ,  $\hat{N} = \hat{L}^\dagger \hat{L}$  and  $\hat{M} = \mathbb{I}$

$$\mathcal{E}_{AC2} = -\frac{1}{2\hbar} \text{Tr}(\hat{\sigma}_z^c \hat{\Phi}_6) = -\frac{1}{4\hbar} \left( \text{Tr}(\hat{\theta}_B \hat{L}^\dagger \hat{L} e^{\mathcal{L}t} (\hat{\rho}_{eq} \hat{\theta}_A)) + \text{Tr}(\hat{\theta}_B e^{\mathcal{L}t} (\hat{\theta}_A \hat{\rho}_{eq}) \hat{L}^\dagger \hat{L}) \right) \quad (83)$$

Combining Eq. (82) and Eq. (83) we have

$$\mathcal{E}_{AC1} + \mathcal{E}_{AC2} = -\frac{1}{4\hbar} \text{Tr}(\hat{\theta}_B \{ \hat{L}^\dagger \hat{L}, e^{\mathcal{L}t} (\{\hat{\rho}_{eq}, \hat{\theta}_A\}) \}) \quad (84)$$

Finally for the denominator we have no time evolution with  $\chi = 0$ ,  $\hat{N} = \mathbb{I}$ ,  $\hat{M} = \mathbb{I}$  and we input  $\hat{\theta}_B = \mathbb{I}$ .

$$\mathcal{E}_D = \text{Tr}(\hat{\sigma}_z^c \hat{\Psi}_2) = \frac{1}{2} \left( \text{Tr}(\hat{\rho}_{eq} \hat{\theta}_A) + \text{Tr}(\hat{\theta}_A \hat{\rho}_{eq}) \right). \quad (85)$$

Combining all these terms we can therefore evaluate the transition rate as

$$\dot{C}(t) = \frac{\mathcal{E}_{H1} + \mathcal{E}_{H2} + \mathcal{E}_J + \mathcal{E}_{AC1} + \mathcal{E}_{AC2}}{2 \mathcal{E}_D}. \quad (86)$$

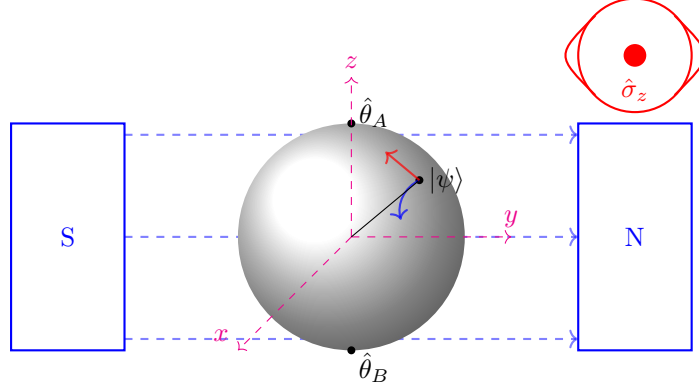


**Fig. 13:** Bloch sphere dynamics of a spin-1/2 system in Eq. (87), magnetic field rotates around  $y$ -axis while  $z$ -axis measurement drives the system towards the nearest pole. If  $\mu \ll \gamma$ , the system exhibits metastable transitions between the two poles ( $\hat{\theta}_A$  and  $\hat{\theta}_B$ ).

### Decohering spin-1/2 transitions

A simple open quantum system to study the transition rate is a single spin-1/2 system with a magnetic field and continuous measurements as shown in Fig. 13. The magnetic field along the  $y$ -axis causes the spin state to precess around the  $y$ -axis, whereas the measurement in the  $z$ -direction localises the system at a pole, most likely the nearest one. Thus, its Lindblad equation in Eq. (54) is given with Hamiltonian and Lindbladian operators

$$\hat{H} = \mu \hat{\sigma}_y \quad \text{and} \quad \hat{L} = \sqrt{\gamma} \hat{\sigma}_z. \quad (87)$$

In particular, when  $\mu$  is significantly smaller than  $\gamma$ , this system exhibits metastable transitions between the two poles

$$\hat{\theta}_A = |0\rangle \langle 0| \quad \text{and} \quad \hat{\theta}_B = |1\rangle \langle 1|. \quad (88)$$

Note that the stationary/equilibrium state of this system is the fully mixed state  $\hat{\rho}_{eq} = (|0\rangle \langle 0| + |1\rangle \langle 1|) / 2$ . Then, we can analytically solve these Lindblad dynamics for the correlation function and its rate expressions such as

$$C(t) = \frac{1}{2} \left( 1 - e^{-\frac{\gamma}{\hbar} t} \left( \cosh(\omega t) + \frac{\gamma}{\hbar \omega} \sinh(\omega t) \right) \right), \quad (89)$$

$$\dot{C}(t) = \frac{2\mu^2}{\hbar^2 \omega} e^{-\frac{\gamma}{\hbar} t} \sinh(\omega t), \quad (90)$$

with  $\omega = \sqrt{(\gamma^2 - 4\mu^2)/\hbar^2}$ .

Table 2 presents the analytical expressions for all terms that contribute to the correlation function. Among the four contributions to the overall rate, the combinations  $\hat{\rho}_{eq} = |1\rangle \langle 1|$  with  $\hat{\theta}_A = \mathbb{I}$  and  $\hat{\rho}_{eq} = |1\rangle \langle 1|$  with  $\hat{\theta}_A = \hat{\sigma}_z$  exactly cancel each other out exactly. The remaining two combinations,  $\hat{\rho}_{eq} = |0\rangle \langle 0|$  with  $\hat{\theta}_A = \mathbb{I}$  and  $\hat{\rho}_{eq} = |0\rangle \langle 0|$



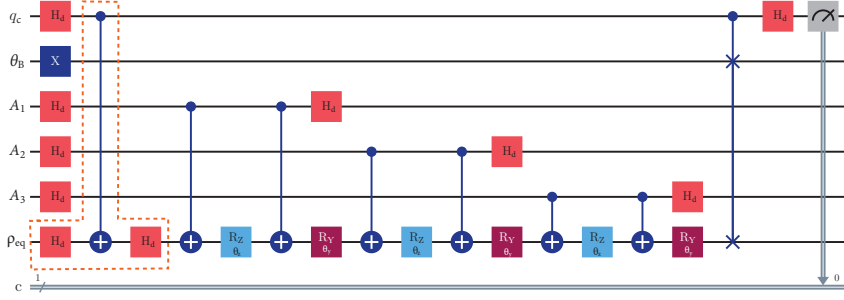


**Fig. 14:** The six-qubit circuit for computing  $\mathcal{E}_C$ . The three ancillary qubits,  $A_1$ – $A_3$ , facilitate Schrödinger-Lindblad time evolution. All qubits are initialised in  $|0\rangle$ . The gates within the dashed box correspond to the case of  $\hat{\theta}_A = \hat{\sigma}_z$ , and the gates are omitted for  $\hat{\theta}_A = \mathbb{I}$ . The 1-qubit gates are parametrised with  $\hat{R}_z(\theta_z)$  and  $\hat{R}_y(\theta_y)$  in  $\hat{\rho}_{eq}$ .

with  $\hat{\theta}_A = \hat{\sigma}_z$ , yield identical contributions. This allows us to perform one of the quantum circuits only with  $\hat{\rho}_{eq} = |0\rangle\langle 0|$  to compute the correlation function  $C(t)$ .

Table 1 in the main text gives analytic expressions for all terms contributing to the time derivative of the correlation function. We observe cancellation between the jump and anti-commutator contributions, with the Hamiltonian parts  $\mathcal{E}_{H1}$  and  $\mathcal{E}_{H2}$  giving identical contributions that sum to give the rate (when divided by  $2\langle\hat{\theta}_A\rangle_{eq}$ ). We can thus calculate the correlation derivative as

$$\dot{C}(t) = 2\mathcal{E}_{H1}(t), \quad (91)$$

for the spin-1/2 model. This simplification arises from the inherent properties of the spin-1/2 system.

$\hat{\rho}_{eq}$	$\hat{\theta}_A$	$\mathcal{E}$
$ 0\rangle\langle 0 $	$\mathbb{I}$	$\frac{1}{2} \left( 1 - e^{-\frac{\gamma}{\hbar}t} \left( \cosh(\omega t) + \frac{\gamma}{\hbar\omega} \sinh(\omega t) \right) \right)$
$ 0\rangle\langle 0 $	$\hat{\sigma}_z$	$\frac{1}{2} \left( 1 - e^{-\frac{\gamma}{\hbar}t} \left( \cosh(\omega t) + \frac{\gamma}{\hbar\omega} \sinh(\omega t) \right) \right)$
$ 1\rangle\langle 1 $	$\mathbb{I}$	$\frac{1}{2} \left( 1 + e^{-\frac{\gamma}{\hbar}t} \left( \cosh(\omega t) + \frac{\gamma}{\hbar\omega} \sinh(\omega t) \right) \right)$
$ 1\rangle\langle 1 $	$\hat{\sigma}_z$	$-\frac{1}{2} \left( 1 + e^{-\frac{\gamma}{\hbar}t} \left( \cosh(\omega t) + \frac{\gamma}{\hbar\omega} \sinh(\omega t) \right) \right)$

**Table 2:** Analytic expectation value expressions contributing to the correlation function in Eq. (89) for the decohering spin-1/2 model with Eq. (87).

## Experimental results from IBMQ

We here present a more detailed account of the spin-1/2 correlation function and its rate experiments. In Figs. 14 and 15, we give the quantum circuits for computing the

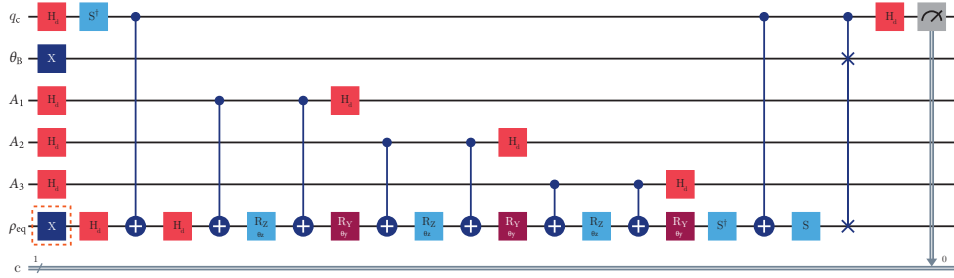


**Fig. 15:** The six-qubit circuit for computing  $\mathcal{E}_{\tilde{H}_1}$ . All qubits are initialised in  $|0\rangle$ , and the three ancillary qubits  $A_1 - A_3$  are for the Schrödinger-Lindblad time evolution. The  $\hat{\sigma}_x$  gate within the dashed box is put for  $\hat{\rho}_{eq} = |1\rangle\langle 1|$  while this gate is removed for  $\hat{\rho}_{eq} = |0\rangle\langle 0|$ .

$t$	0.0	0.2	0.4	0.6	0.8	1.0
$\theta_z$	0	$\frac{2}{\sqrt{15}}$	$\frac{2\sqrt{2}}{\sqrt{15}}$	$\frac{2\sqrt{3}}{\sqrt{15}}$	$\frac{4}{\sqrt{15}}$	$\frac{2\sqrt{5}}{\sqrt{15}}$
$\theta_y$	0	$\frac{1}{75}$	$\frac{2}{75}$	$\frac{3}{75}$	$\frac{4}{75}$	$\frac{5}{75}$

**Table 3:** The rotation gate parameters  $\theta_z$  and  $\theta_y$  are used in Figs. 14 and 15 for the various evolution times. The parameters are  $\gamma = 1$  and  $\mu = 0.1$  for our experiments.

correlation function and the rate respectively. The single-qubit rotation angles,  $\theta_z(t)$  and  $\theta_y(t)$ , are determined by the Hamiltonian and Lindbladian parameters in the time evolution gates such as

$$\theta_z(t) = 2\sqrt{\frac{\gamma t}{N}} \quad \text{and} \quad \theta_y(t) = 2\frac{\mu t}{N}, \quad (92)$$

where  $N$  denotes either the number of ancillary qubits used or the number of time-evolution iterations if the qubits are recycled. The specific values for the experiments are given in Table 3.

Tables 4 and 5 show the raw data from the correlation function and the rate simulations using the *ibm\_brisbane* quantum processor. These original experimental data sets are plotted in Fig. 6 in the main text. In Figs. 16 (a) and (b), we re-plot the experimental data of  $C(t)$  and  $\dot{C}(t)$  on the *ibm\_brisbane* quantum processor with systematic shifts, along with the analytical solutions and ideal quantum numerical simulations. In Figs. 16 (a) and (b), we systematically shifted the the experimental result to set zero at  $t = 0$  while the unshifted versions of these figures are shown in the main text. The shifted curves show the experimental results are very closely matched with the results of the ideal six-qubit quantum simulation (red dashed line) with small deviations. This implies that the shifted value of  $\dot{C}(0)$  is determined by the amount of

	$t_0 = 0.0$			$t_0 = 0.2$		
<b>Attempt</b>	$\hat{\theta}_A = \mathbb{I}$	$\hat{\theta}_A = \hat{\sigma}_z$	$\mathcal{E}_C$	$\hat{\theta}_A = \mathbb{I}$	$\hat{\theta}_A = \hat{\sigma}_z$	$\mathcal{E}_C$
1	5266	5222	0.0488	6199	5094	0.1293
2	6243	4605	0.0848	5727	4944	0.0671
3	6560	4984	0.1544	5008	5110	0.0118
4	2267	5065	-0.2668	5028	5841	0.0869
5	5198	5001	0.0199	3140	4978	-0.1882
6	5533	3884	-0.0583	5590	4512	0.0102
7	5121	5248	0.0369	5470	4953	0.0423
8	5608	5171	0.0779	5050	5833	0.0883
9	5320	5229	0.0549	5299	5257	0.0556
10	3964	5268	-0.0768	5276	5335	0.0611
<b>Mean</b>			<b>0.00757</b>			<b>0.03644</b>
<b>SEM</b>			<b>0.03714</b>			<b>0.02740</b>
	$t_0 = 0.4$			$t_0 = 0.6$		
<b>Attempt</b>	$\hat{\theta}_A = \mathbb{I}$	$\hat{\theta}_A = \hat{\sigma}_z$	$\mathcal{E}_C$	$\hat{\theta}_A = \mathbb{I}$	$\hat{\theta}_A = \hat{\sigma}_z$	$\mathcal{E}_C$
1	5102	5424	0.0526	4937	4925	-0.0138
2	5103	5307	0.0410	5133	5671	0.0804
3	4325	5928	0.0253	5317	5071	0.0388
4	5296	5275	0.0571	4293	5992	0.0285
5	5094	5555	0.0649	5615	5714	0.1329
6	4570	5193	-0.0237	6022	5133	0.1155
7	5537	5257	0.0794	5775	4378	0.0153
8	5547	4884	0.0431	4943	4972	-0.0085
9	5251	5406	0.0657	5740	4813	0.0553
10	5056	4973	0.0029	5493	5437	0.0930
<b>Mean</b>			<b>0.04083</b>			<b>0.05374</b>
<b>SEM</b>			<b>0.00997</b>			<b>0.01602</b>
	$t_0 = 0.8$			$t_0 = 1.0$		
<b>Attempt</b>	$\hat{\theta}_A = \mathbb{I}$	$\hat{\theta}_A = \hat{\sigma}_z$	$\mathcal{E}_C$	$\hat{\theta}_A = \mathbb{I}$	$\hat{\theta}_A = \hat{\sigma}_z$	$\mathcal{E}_C$
1	5207	6216	0.1423	5207	5840	0.1047
2	5483	5104	0.0587	6401	5823	0.2224
3	4426	5008	-0.0566	5868	5035	0.0903
4	5972	5258	0.1230	4350	5438	-0.0212
5	4899	6220	0.1119	5276	5110	0.0386
6	5698	5682	0.1380	5086	5102	0.0188
7	5066	4859	-0.0075	4901	4494	-0.0605
8	5379	5331	0.0710	5174	5347	0.0521
9	6248	4765	0.1013	5142	5405	0.0547
10	5272	5341	0.0613	4392	5285	-0.0323
<b>Mean</b>			<b>0.07434</b>			<b>0.04676</b>
<b>SEM</b>			<b>0.02040</b>			<b>0.02569</b>

**Table 4:** IBMQ data for  $C(t)$  with  $t = \{0, 0.2, 0.4, 0.6, 0.8, 1.0\}$  and  $\hat{\rho}_{eq} = |0\rangle\langle 0|$ . These ten data sets are performed with the circuits in Fig. 15 (each set for 20,000 shots). The data of the  $\hat{\theta}_A$  columns represent the counts with measurement outcome  $|0\rangle$  in the control qubit and  $\hat{\rho}_{eq} = |0\rangle\langle 0|$ , as the contributions of  $\hat{\rho}_{eq} = |1\rangle\langle 1|$  cancel each other.

gate and measurement errors at  $t = 0$  without the modular Lindblad time evolution circuit on the IBMQ device.

	$t_0 = 0.0$			$t_0 = 0.2$		
<b>Attempt</b>	$\hat{\rho}_{eq} =  0\rangle\langle 0 $	$\hat{\rho}_{eq} =  1\rangle\langle 1 $	$\mathcal{E}_{H1}$	$\hat{\rho}_{eq} =  0\rangle\langle 0 $	$\hat{\rho}_{eq} =  1\rangle\langle 1 $	$\mathcal{E}_{H1}$
1	4816	5087	-0.0009700	5218	4787	0.00005000
2	4873	5117	-0.0001000	5335	4980	0.003150
3	4840	5050	-0.001100	5283	4809	0.0009200
4	4874	5083	-0.0004300	4868	5166	0.0003400
5	4863	5018	-0.001190	5283	4984	0.002670
<b>Mean</b>			<b>-0.0007580</b>			<b>0.001426</b>
<b>SEM</b>			<b>0.0002108</b>			<b>0.0006264</b>
	$t_0 = 0.4$			$t_0 = 0.6$		
<b>Attempt</b>	$\hat{\rho}_{eq} =  0\rangle\langle 0 $	$\hat{\rho}_{eq} =  1\rangle\langle 1 $	$\mathcal{E}_{H1}$	$\hat{\rho}_{eq} =  0\rangle\langle 0 $	$\hat{\rho}_{eq} =  1\rangle\langle 1 $	$\mathcal{E}_{H1}$
1	5339	4834	0.001730	5316	4843	0.001590
2	5435	4929	0.003640	5299	5084	0.003830
3	5368	4834	0.002020	5422	4886	0.003080
4	5404	4866	0.002700	5309	4966	0.002750
5	5351	5032	0.003830	5332	4950	0.002820
<b>Mean</b>			<b>0.002784</b>			<b>0.002814</b>
<b>SEM</b>			<b>0.0004200</b>			<b>0.0003609</b>
	$t_0 = 0.8$			$t_0 = 1.0$		
<b>Attempt</b>	$\hat{\rho}_{eq} =  0\rangle\langle 0 $	$\hat{\rho}_{eq} =  1\rangle\langle 1 $	$\mathcal{E}_{H1}$	$\hat{\rho}_{eq} =  0\rangle\langle 0 $	$\hat{\rho}_{eq} =  1\rangle\langle 1 $	$\mathcal{E}_{H1}$
1	5196	5020	0.002160	5573	4892	0.004650
2	5374	4941	0.003150	5413	4998	0.004110
3	5327	4962	0.002890	5420	5004	0.004240
4	5299	4918	0.002170	5314	4884	0.001980
5	5512	4962	0.004740	5157	5392	0.005490
<b>Mean</b>			<b>0.003022</b>			<b>0.004094</b>
<b>SEM</b>			<b>0.0004719</b>			<b>0.0005809</b>

**Table 5:** IBMQ data for  $\dot{C}(t)$ : For each value of  $t = \{0, 0.2, 0.4, 0.6, 0.8, 1\}$  and  $\hat{\rho}_{eq} = |0\rangle\langle 0|$  or  $|1\rangle\langle 1|$ , the five set of the circuits in Fig. 15 were performed and each set is made with 10,000 shots. The values in the  $\hat{\rho}_{eq} = |0\rangle\langle 0|$  and  $\hat{\rho}_{eq} = |1\rangle\langle 1|$  represent the counts with measurement outcome  $|0\rangle$  in the control qubit. Each pair in these two columns is used to calculate the expectation values  $\mathcal{E}_{H1}$ .

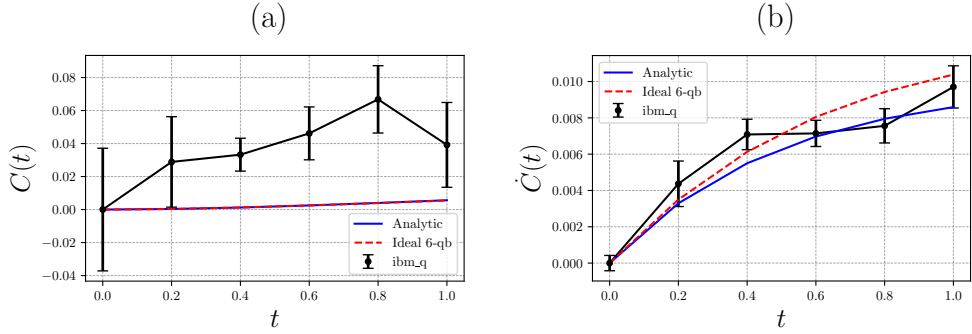


**Fig. 16:** The shifted experimental data of  $C(t)$  in (a) and  $\dot{C}(t)$  in (b) compared to the analytic solution and the ideal six-qubit circuit. For both panels, the parameters are  $\mu = 0.1$ ,  $\gamma = 1$ , and  $\hbar = 1$  and plots are systematically shifted to set  $C(0) = 0$  and  $\dot{C}(0) = 0$  while the unshifted plots are presented in the main text. The original experimental data in (a) and (b) are given in Tables 4 and 5.

## Modular Lindblad evolution circuits

### Schrödinger picture state evolution

Here, we recap the Lindblad state evolution scheme in the Schrödinger picture described by Cleve and Wang in [22]. In their approach, time is discretised into  $N$  segments and an ancillary qudit with dimension  $d + 1$  is required where  $d$  is the number of Lindblad operators. The qudit state  $\hat{\rho}_A$  is initially prepared in

$$\hat{\rho}_A = |0_{d+1}\rangle \langle 0_{d+1}|. \quad (93)$$

Using qubit architectures, if  $d + 1$  is not a power of two, the qudit can be embedded into a qubit-based register with dimension  $2^n \geq d + 1$  for  $n$  qubits. The combined system undergoes the joint unitary evolution under the Hamiltonian-like operator

$$\hat{J} = \begin{pmatrix} 0 & \hat{L}_1^\dagger & \cdots & \hat{L}_d^\dagger \\ \hat{L}_1 & \ddots & & 0 \\ \vdots & & \ddots & \vdots \\ \hat{L}_d & 0 & \cdots & 0 \end{pmatrix}, \quad (94)$$

for the time duration of  $\sqrt{\delta}$ , where  $\delta = \tau/N$ . After the ancillary qubit is traced out as shown in Fig. 17, the remaining reduced density matrix is evolved under  $\hat{H}$  for time step  $\delta$ . This process is repeated  $N$  times to simulate the approximate Lindblad dynamics with accuracy increasing with  $N$ .

For the first stage, in block matrix notation, the total input state is given by  $|0_{d+1}\rangle \langle 0_{d+1}| \otimes \hat{\rho}$ . The joint unitary evolution is given by

$$\begin{aligned} e^{-i\hat{J}\sqrt{\delta}} (|0_{d+1}\rangle \langle 0_{d+1}| \otimes \hat{\rho}) e^{i\hat{J}\sqrt{\delta}} &\approx |0_{d+1}\rangle \langle 0_{d+1}| \otimes \hat{\rho} - i \left[ \hat{J}, (|0_{d+1}\rangle \langle 0_{d+1}| \otimes \hat{\rho}) \right] \sqrt{\delta} \\ &+ \left( \hat{J} (|0_{d+1}\rangle \langle 0_{d+1}| \otimes \hat{\rho}) \hat{J} - \frac{1}{2} \hat{J}^2 (|0_{d+1}\rangle \langle 0_{d+1}| \otimes \hat{\rho}) - \frac{1}{2} (|0_{d+1}\rangle \langle 0_{d+1}| \otimes \hat{\rho}) \hat{J}^2 \right) \delta \\ &+ O(\delta^{3/2}). \end{aligned} \quad (95)$$

The only non-zero entries of the commutator term are off-diagonal in the tensor product representation. The reduced density matrix after tracing out the ancillary channel

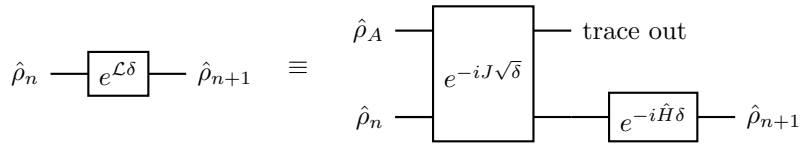


**Fig. 17:** Schrödinger picture density matrix evolution circuit [22]

can be evolved under the Hamiltonian  $\hat{H}$ , giving

$$\hat{\rho} \rightarrow \hat{\rho} - i[\hat{H}, \hat{\rho}]\delta + \sum_{k=1}^d \left( \hat{L}_k \hat{\rho} \hat{L}_k^\dagger - \frac{1}{2} \hat{L}_k^\dagger \hat{L}_k \hat{\rho} - \frac{1}{2} \hat{\rho} \hat{L}_k^\dagger \hat{L}_k \right) \delta + O(\delta^{3/2}). \quad (96)$$

Taking this output density matrix and feeding it back into the Lindblad evolution circuit for  $N$  iterations, it approximately becomes the time-evolved density matrix  $\hat{\rho}(\tau)$ .

### Heisenberg picture operator evolution

Here we give a more detailed derivation of the scheme for the quantum simulation of Heisenberg picture Lindblad dynamics in the main text. This scheme is inspired by the previous evolution method and essentially shows a time reversal of the above algorithm. Unlike the algorithm in [22], this Heisenberg-Lindblad evolution scheme is conditional and has a success probability depending on  $N$  iterations. First, we define a time step by discretising the evolution time into  $N$  segments. Then we prepare an ancillary qudit register of dimension  $d+1$ , where  $d$  is the number of Lindblad operators, in the fully mixed state

$$\hat{\rho}_A = \frac{1}{d+1} \left( \sum_{n=0}^d |n_{d+1}\rangle \langle n_{d+1}| \right). \quad (97)$$

The qudit  $\hat{\rho}_A$  and  $\hat{\theta}_n$  undergoes the joint unitary evolution under the same operator  $\hat{J}$  in Eq. (94). Then, we need to project onto the  $|0_{d+1}\rangle \langle 0_{d+1}|$  subspace of the ancillary qudit, and the remaining reduced density matrix is evolved under  $-\hat{H}$  for time step  $\delta$ . This process is repeated  $N$  times to approximate the Lindblad dynamics for large  $N$ . We first have the total input state  $\hat{\rho}_A \otimes \hat{\theta}_n$ , and the joint evolution is given by

$$\begin{aligned} e^{-i\hat{J}\sqrt{\delta}} \left( \hat{\rho}_A \otimes \hat{\theta}_n \right) e^{i\hat{J}\sqrt{\delta}} &\approx \hat{\rho}_A \otimes \hat{\theta}_n - i \left[ \hat{J}, \left( \hat{\rho}_A \otimes \hat{\theta}_n \right) \right] \sqrt{\delta} \\ &+ \left( \hat{J} \left( \hat{\rho}_A \otimes \hat{\theta}_n \right) \hat{J} - \frac{1}{2} \hat{J}^2 \left( \hat{\rho}_A \otimes \hat{\theta}_n \right) - \frac{1}{2} \left( \hat{\rho}_A \otimes \hat{\theta}_n \right) \hat{J}^2 \right) \delta \\ &+ O(\delta^{3/2}). \end{aligned} \quad (98)$$

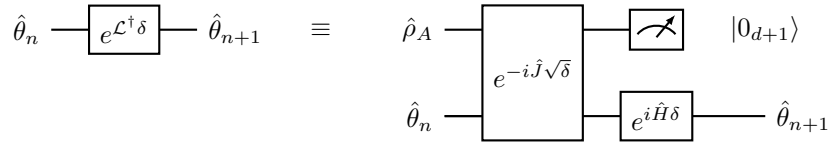


**Fig. 18:** Heisenberg picture observable evolution circuit. The success of each cycle is conditional on  $|0_{d+1}\rangle$  being recorded as a result of the ancillary qubit measurements.

The only non-zero entries of the commutator term are off-diagonal in the tensor product representation. In the second-order term, we find that the component of  $|0_{d+1}\rangle\langle 0_{d+1}|$  in the ancillary qudit is given by

$$\begin{aligned} & \left( \hat{J}(\hat{\rho}_A \otimes \hat{\theta}_n)\hat{J} - \frac{1}{2}\hat{J}^2(\hat{\rho}_A \otimes \hat{\theta}_n) - \frac{1}{2}(\hat{\rho}_A \otimes \hat{\theta}_n)\hat{J}^2 \right)_{00} \\ &= \frac{1}{d+1} \sum_{k=1}^d \left( \hat{L}_k^\dagger \hat{\theta}_n \hat{L}_k - \frac{1}{2} \hat{L}_k^\dagger \hat{L}_k \hat{\theta}_n - \frac{1}{2} \hat{\theta}_n \hat{L}_k^\dagger \hat{L}_k \right). \end{aligned} \quad (99)$$

Therefore, we can measure the ancillary channel with the measurement outcome  $|0_{d+1}\rangle$ , and the state is evolved with a single  $\delta$  time step for the dissipative component of the dynamics such as

$$\hat{\theta}_n \rightarrow \hat{\theta}_n + \sum_{k=1}^d \left( \hat{L}_k^\dagger \hat{\theta}_n \hat{L}_k - \frac{1}{2} \hat{L}_k^\dagger \hat{L}_k \hat{\theta}_n - \frac{1}{2} \hat{\theta}_n \hat{L}_k^\dagger \hat{L}_k \right) \delta. \quad (100)$$

Taking the above result and evolving under the sign-flipped Hamiltonian ( $-\hat{H}$ ), we have

$$\hat{\theta}_n \rightarrow \hat{\theta}_n + i[\hat{H}, \hat{\theta}_n]\delta + \sum_{k=1}^d \left( \hat{L}_k^\dagger \hat{\theta}_n \hat{L}_k - \frac{1}{2} \hat{L}_k^\dagger \hat{L}_k \hat{\theta}_n - \frac{1}{2} \hat{\theta}_n \hat{L}_k^\dagger \hat{L}_k \right) \delta + O(\delta^{3/2}). \quad (101)$$

Finally, we use the output state and feed it back into the circuit for  $N$  successful iterations, the state approximates the time-evolved observable  $\hat{\theta}(\tau)$  for a given time period  $\tau$ .

## Quantum Brownian motion in a 1D double well

Caldeira and Leggett derived the master equation that governs the evolution of the reduced density operators of a quantum particle coupled to a bath of thermal oscillators [45]. This Caldeira-Leggett (CL) master equation is expressed with  $\hat{H}_{CL} = \hat{P}^2/(2m) + V(\hat{X})$

$$\frac{d}{dt}\hat{\rho}_s = -\frac{i}{\hbar}[\hat{H}_{CL}, \hat{\rho}_s] - \frac{i\gamma}{\hbar}[\hat{X}, \{\hat{P}, \hat{\rho}_s\}] - \frac{2m\gamma k_B T}{\hbar^2}[\hat{X}, [\hat{X}, \hat{\rho}_s]], \quad (102)$$

where  $\hat{X}$  and  $\hat{P}$  are the position and momentum operators of the quantum particle.

As first detailed in [45] and more pedagogically in [46, 62], the CL master equation can be derived by considering a central system oscillator with the Hamiltonian

$$\hat{H}_s = \frac{\hat{P}^2}{2m} + \frac{1}{2}m\omega^2\hat{X}^2, \quad (103)$$

and a bath of oscillators described by the environmental Hamiltonian

$$\hat{H}_e = \sum_i \left( \frac{\hat{p}_i^2}{2m_i} + \frac{1}{2} m_i \omega_i^2 \hat{q}_i^2 \right), \quad (104)$$

which represents a collection of harmonic oscillators, each characterized by mass  $m_i$ , frequency  $\omega_i$ , position operator  $\hat{q}_i$ , and momentum operator  $\hat{p}_i$ . The interaction between the system and the environment is captured by the interaction Hamiltonian

$$\hat{H}_{\text{int}} = \hat{X} \otimes \sum_i c_i \hat{q}_i, \quad (105)$$

where  $\hat{X}$  couples to  $\hat{q}_i$  with coupling strength  $c_i$ . By tracing out the environmental degrees of freedom and applying the high temperature and Markovian approximations, we arrive at the CL master equation in Eq. (102).

The CL dynamics does not maintain the positivity of the density matrix, especially at reduced temperatures. Addressing this limitation, a modification in Ref. [46] introduces a new term such as

$$-\frac{\gamma}{8mk_B T} [\hat{P}, [\hat{P}, \hat{\rho}_S]], \quad (106)$$

which becomes insignificant at elevated temperatures. This ensures the positivity of the density matrix, thereby allowing the equation to be recast in the positivity preserving Lindblad form [48, 63]

$$\frac{d}{dt} \hat{\rho}_S = -\frac{i}{\hbar} [\hat{H}_\gamma, \hat{\rho}_S] + \frac{1}{\hbar} \left( \hat{L}_\gamma \hat{\rho}_S \hat{L}_\gamma^\dagger - \frac{1}{2} \{ \hat{\rho}_S, \hat{L}_\gamma^\dagger \hat{L}_\gamma \} \right), \quad (107)$$

with  $\lambda_T = \sqrt{\hbar/4mk_B T}$ . Its Hamiltonian and Lindblad operators are

$$\hat{H}_\gamma = \frac{\hat{P}^2}{2m} + \hat{V}(\hat{X}) + \frac{\gamma}{2} (\hat{X} \hat{P} + \hat{P} \hat{X}), \quad \text{and} \quad \hat{L}_\gamma = \sqrt{\gamma} \left( \lambda_T^{-1} \hat{X} + i \lambda_T \hat{P} \right). \quad (108)$$

In the grid point method, we use a discrete position representation and the wave function with  $n$  qubits is given over the coordinate interval  $x \in [0, 1 - 2^{-n}]$  using QuTiP [52]. The position operator is defined as

$$\hat{X} = \sum_{k=0}^{2^n-1} x_k |x_k\rangle \langle x_k|, \quad (109)$$

This position space grid induces a momentum grid that satisfies the discrete uncertainty relation, known as the error-disturbance uncertainty relation [64],  $\delta x \delta p = 2\pi\hbar/2^n$  implying momentum spacing  $\delta p = 2\pi\hbar$ . Then, the momentum eigenstates have



eigenvalues  $p_j = (-2^{n-1} + j)\delta p$  for  $j = 0, 1, \dots, 2^n - 1$  and the momentum operator is defined as

$$\hat{P} = \sum_{j=0}^{2^n-1} p_j |p_j\rangle \langle p_j| = \sum_{j,k,l=0}^{2^n-1} p_j \tilde{U}_{jk} |x_k\rangle \langle x_l| \tilde{U}_{lj}^\dagger, \quad (110)$$

where the unitary matrix  $\tilde{U}$  is related to the quantum Fourier transform:

$$\tilde{U}_{jk} = \frac{1}{\sqrt{2^n}} \exp\left(\frac{i}{\hbar} x_j p_k\right). \quad (111)$$

### Controlled-SWAP gate for mixed states

In this section we define a controlled-SWAP (C-SWAP) for two density operators on  $\hat{A} \otimes \hat{B}$ . Suppose we have the following two density operators such as

$$\hat{A} = \sum_{ij} a_{ij} |i\rangle \langle j|, \quad \text{and} \quad \hat{B} = \sum_{kl} b_{kl} |k\rangle \langle l|. \quad (112)$$

The control qubit can be expressed in four components such as  $|0\rangle \langle 0|$ ,  $|0\rangle \langle 1|$ ,  $|1\rangle \langle 0|$ , and  $|1\rangle \langle 1|$ . The first and last components, when combined with the C-SWAP circuit, result in  $|0\rangle \langle 0| \otimes \hat{A} \otimes \hat{B}$  and  $|1\rangle \langle 1| \otimes \hat{B} \otimes \hat{A}$ . If we consider the control input  $|1\rangle \langle 0|$ , the outcome is given by

$$\mathbf{C}_{\text{SWAP}} \left( |1\rangle \langle 0| \otimes \left( \sum_{ijkl} a_{ij} b_{kl} |i\rangle \langle j| \otimes |k\rangle \langle l| \right) \right) = |1\rangle \langle 0| \otimes \left( \sum_{ijkl} a_{ij} b_{kl} |k\rangle \langle j| \otimes |i\rangle \langle l| \right). \quad (113)$$

Similarly, for the control input  $|0\rangle \langle 1|$ , we have

$$\mathbf{C}_{\text{SWAP}} \left( |0\rangle \langle 1| \otimes \left( \sum_{ijkl} a_{ij} b_{kl} |i\rangle \langle j| \otimes |k\rangle \langle l| \right) \right) = |0\rangle \langle 1| \otimes \left( \sum_{ijkl} a_{ij} b_{kl} |i\rangle \langle l| \otimes |k\rangle \langle j| \right). \quad (114)$$

These states are entangled and cannot be simply expressed in terms of the original operators  $\hat{A}$  and  $\hat{B}$ . However, if we take the partial trace over the  $\hat{A}$  and  $\hat{B}$  channels, the resulting states are

$$\text{Tr}(\hat{A}\hat{B}) |1\rangle \langle 0| \quad \text{and} \quad \text{Tr}(\hat{A}\hat{B}) |0\rangle \langle 1| \quad (115)$$

respectively for each choice of control qubit. In this way, the C-SWAP operation allows the multiplication of the two channels. To allow us to keep track of swapped states without expanding into a basis, we define a new notation for the state as referenced in Eq. (113) as follows

$$\sum_{ijkl} a_{ij} b_{kl} |k\rangle \langle j| \otimes |i\rangle \langle l| = \hat{A} \overset{\otimes}{\underset{k}{\leftarrow}} \hat{B}, \quad (116)$$

where the “k” signifies that we are swapping the ket parts of the projectors. Similarly, for the state referenced in Eq. (114), we have

$$\sum_{ijkl} a_{ij} b_{kl} |i\rangle \langle l| \otimes |k\rangle \langle j| = \hat{A} \overset{\otimes}{\underset{b}{\leftarrow}} \hat{B} \quad (117)$$

where “b” denotes a bra part swap. After the C-SWAP gate, we have the output states

$$|0\rangle \langle 0| \otimes \hat{A} \otimes \hat{B} \otimes \hat{C} \rightarrow |0\rangle \langle 0| \otimes \hat{A} \otimes \hat{C} \otimes \hat{B}, \quad (118)$$

$$|1\rangle \langle 1| \otimes \hat{A} \otimes \hat{B} \otimes \hat{C} \rightarrow |1\rangle \langle 1| \otimes \hat{B} \otimes \hat{A} \otimes \hat{C}, \quad (119)$$

$$|0\rangle \langle 1| \otimes \hat{A} \otimes \hat{B} \otimes \hat{C} \rightarrow |0\rangle \langle 1| \otimes \left( \hat{A} \overset{\otimes}{\underset{b_1}{\leftarrow}} \hat{B} \right) \overset{\otimes}{\underset{b_2}{\leftarrow}} \hat{C}, \quad (120)$$

$$|1\rangle \langle 0| \otimes \hat{A} \otimes \hat{B} \otimes \hat{C} \rightarrow |1\rangle \langle 0| \otimes \left( \hat{A} \overset{\otimes}{\underset{k_1}{\leftarrow}} \hat{B} \right) \overset{\otimes}{\underset{k_2}{\leftarrow}} \hat{C}. \quad (121)$$

Taking the trace-out of the state of  $|0\rangle \langle 1|$ , we have

$$\text{Tr} \left( \sum_{ijklmn} a_{ij} b_{kl} c_{mn} |i\rangle \langle l| \otimes |m\rangle \langle j| \otimes |k\rangle \langle n| \right) = \text{Tr}(\hat{B} \hat{A} \hat{C}). \quad (122)$$

Similarly, the trace-out of the state of  $|1\rangle \langle 0|$  gives

$$\text{Tr} \left( \sum_{ijklmn} a_{ij} b_{kl} c_{mn} |k\rangle \langle j| \otimes |i\rangle \langle n| \otimes |m\rangle \langle l| \right) = \text{Tr}(\hat{A} \hat{B} \hat{C}). \quad (123)$$